New Journal of Physics
The open access journal at the forefront of physics

Deutsche Physikalische Gesellschaft DPG IOP Institute of Physics

PAPER • OPEN ACCESS

Dynamics of atoms within atoms

To cite this article: S Tiwari *et al* 2022 *New J. Phys.* **24** 073005

New Journal of Physics
The open access journal at the forefront of physics

Deutsche Physikalische Gesellschaft DPG
IOP Institute of Physics

Published in partnership with: Deutsche Physikalische Gesellschaft and the Institute of Physics

OPEN ACCESS

RECEIVED
9 November 2021

REVISED
14 June 2022

ACCEPTED FOR PUBLICATION
17 June 2022

PUBLISHED
6 July 2022

PAPER

Dynamics of atoms within atoms

S Tiwari[1,*], F Engel[2], M Wagner[3,4], R Schmidt[3,4], F Meinert[2] and S Wüster[1,*]

[1] Department of Physics, Indian Institute of Science Education and Research, Bhopal, Madhya Pradesh 462 066, India
[2] Physikalisches Institut and Center for Integrated Quantum Science and Technology, Universität Stuttgart, Pfaffenwaldring 57, 70569 Stuttgart, Germany
[3] Max-Planck-Institute of Quantum Optics, Hans-Kopfermann-Straße 1, 85748 Garching, Germany
[4] Munich Center for Quantum Science and Technology (MCQST), Schellingstr. 4, D-80799 München, Germany
[*] Authors to whom any correspondence should be addressed.

E-mail: shiva17@iiserb.ac.in and sebastian@iiserb.ac.in

Keywords: Rydberg atoms, Bose–Einstein condensate, Rydberg-BEC interaction, quantum impurity, Bogoliubov excitations, beyond mean-field

Supplementary material for this article is available online

Abstract

Recent experiments with Bose–Einstein condensates have entered a regime in which thousands of ground-state condensate atoms fill the Rydberg-electron orbit. After the excitation of a single atom into a highly excited Rydberg state, scattering off the Rydberg electron sets ground-state atoms into motion, such that one can study the quantum-many-body dynamics of atoms moving within the Rydberg atom. Here we study this many-body dynamics using Gross–Pitaevskii and truncated Wigner theory. Our simulations focus in particular on the scenario of multiple sequential Rydberg excitations on the same rubidium condensate which has become the standard tool to observe quantum impurity dynamics in Rydberg experiments. We investigate to what extent such experiments can be sensitive to details in the electron–atom interaction potential, such as the rapid radial modulation of the Rydberg molecular potential, or p-wave shape resonance. We demonstrate that both effects are crucial for the initial condensate response within the Rydberg orbit, but become less relevant for the density waves emerging outside the Rydberg excitation region at later times. Finally we explore the local dynamics of condensate heating. We find that it provides only minor corrections to the mean-field dynamics. Combining all these insights, our results suggest Bose–Einstein condensates as a viable platform for the *in situ* and real time interrogation of ultra-cold chemistry dynamics involving Rydberg states.

1. Introduction

The study of quantum impurities has become an important branch of ultra-cold atomic physics, allowing explorations of condensed matter phenomena ranging from the Kondo effect [1, 2] over polaron formation [3–7] to the Anderson orthogonality catastrophe [8]. A unique impurity object in this context is a Rydberg atom in a Bose–Einstein condensate (BEC) [4, 9–13]. Due to the extreme radius of the Rydberg electron density distribution $r_{\rm orb} \approx 2a_0 n^2$, which can reach $r_{\rm orb} \approx 1.8\ \mu$m at $n = 133$, one can enter the realm where tens of thousands of ground-state atoms are located inside the Rydberg orbit and can be set into motion by collisions with the Rydberg electron during the life-time of the latter.

The Rydberg electron affects the BEC by imprinting a phase on its mean field wave function at short times, which evolves into density waves at later times. It has been suggested to use these features for tracking the motion, detecting the position and deducing or decohering the quantum state of isolated Rydberg impurities [14–18]. However, for these proposals a detailed understanding of the joint BEC and Rydberg impurity dynamics is required. Experiments probing both to date rely on the repeated excitation of a Rydberg atom at roughly the same location within the laser beam waist [9] and then observe the cumulative effect of these excitations.

In this work we numerically analyse how Rydberg atoms excited within a BEC affect the latter, discussing multiple effects that go beyond earlier studies [13, 16, 19]. Most importantly we segregate the different condensate dynamics induced by the small, highly-oscillatory radial features of the Rydberg-ground-state potential, from the slower dynamics due to the classically averaged potential on larger scales. We also assess the importance of details of the Rydberg-condensate interaction that only occur very close to the ion core, and thus only affect a relatively small fraction of the interaction volume, such as the p-wave shape resonance. Finally, we simulate the local Rydberg induced scattering of atoms from the condensate into the thermal cloud using truncated Wigner theory which allows a separation of condensed and uncondensed components.

Earlier studies have shown that a Rydberg impurity excited in a BEC will result in condensate heating [9, 15, 16] that increases with the number of repeated excitations. Since the Rydberg electron interacts only with the condensate atoms present in its orbit, this effect is, on short time-scales, localized within the orbit, and, as we show here, not strong enough to invalidate mean-field theory. The small scale oscillations of the radial part of the interaction potential between Rydberg electron and condensate lead to fast but weak condensate dynamics within each radial well, concomitant with a slower, much more significant directed inwards motion governed by the potential envelope. Fast dynamics significantly contributes to the envelope of the density for repeated excitations, which makes it important to accurately model the radial part of the impurity potential. Our assessment of the impact of details in the Rydberg-condensate interaction potential is important for future numerical simulations of this problem since those are challenging: the highly oscillatory potential inherited from the Rydberg wavefunction necessitates fine spatial computational grids, while the outwards travelling condensate excitations at later times require a large spatial range.

Information on all the above is require to assess whether the ambient BEC can form a 'bubble-chamber' [20] for ultra-cold atomic physics, through the interaction with which the dynamics of more exotic species, involving Rydberg states, might be observed [9, 15, 16].

This article is organized as follows. We introduce our model of a BEC interacting with a Rydberg impurity via different interaction potentials in section 2, and discuss the scheme for the temporal sequence of exciting Rydberg impurities. We then show in section 3.1 that for a single Rydberg impurity, the condensate displays fast dynamics in the small wells of the s-wave impurity potential and a slow average contraction of the condensate particles towards the excitation region. We further compare in section 3.2 the condensate perturbation caused by different interaction potentials and show that the qualitative signal of the condensate is largely insensitive to these details. Out of three potentials used, we justify the use of a cutoff for the full s + p-wave interaction potential in section 3.3, which has a deep central dip near the ionic core of the Rydberg atom. In section 3.4, we show how the contrast in the condensate response increases through a sequence of multiple Rydberg excitations. We go beyond the mean-field approach in section 4 and show that Rydberg excitations only lead to local heating of the BEC, which, even there, only result minor corrections to mean-field theory. We finally summarize our results in section 5 and give an outlook to future directions.

2. Interactions between Rydberg atom and BEC

We consider a gas of N Rb^{87} atoms with mass m forming a BEC. Among the N atoms at most one atom at a time may be excited to a Rydberg state $|\psi\rangle = |\nu s\rangle$, with principal quantum number ν and angular momentum $l = 0$. In this article, we focus exclusively on $|\psi\rangle = |133s\rangle$. This and other parameter choices later are quite closely constrained by our objective to study a response of the BEC that can be optically resolved *in situ*, using phase-contrast imaging [21]. This necessitates large ν, while remaining low enough to avoid too fast inelastic processes [22]. The Rydberg excitation shall be quite localized near the origin, as sketched in figure 1(a). This can be achieved by using a tightly focussed excitation laser, additionally exploiting the background density dependent energy shift [9], both of which, however, leave a residual uncertainty σ of the impurity position $\mathbf{x}$, which we explicitly take in account in our model. Similar to experiments [9], we shall also consider temporal sequences of single Rydberg excitations with subsequent removal by controlled field ionization. The excitation, short presence and then removal of the Rydberg atom are repeated N_{exc} times (see in figure 1(b)). While the Rydberg atom is present, it remains at the location $\mathbf{x}_n$, where n is the index of the excitation segment.

2.1. Electron–atom scattering

The interaction of the Rydberg impurities with condensate atoms inside their orbit can be well described by the Fermi pseudopotential [23, 24], see appendix B. This leads to an effective potential for a given Rydberg

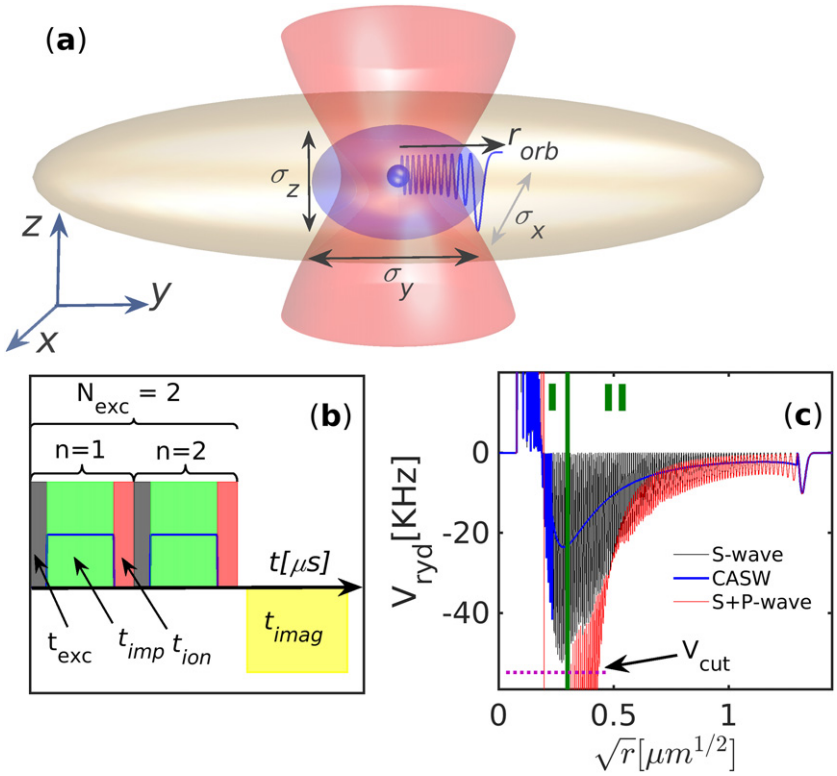

Figure 1. (a) Sketch of localized excitation of a single Rydberg impurity in the BEC. We assume a Rydberg atom of orbital radius $r_{\rm orb}$, with its ionic core (dark blue ball) excited in an excitation region (blue shade) within a cigar-shaped BEC (large ellipsoid), where the red vertical surface represents an equal intensity contour of the laser used to excite the Rydberg atom. The spatial uncertainties of the ion location along the Cartesian directions are σ_x, σ_y and σ_z. (b) Temporal excitation sequence: we assume it takes a time $t_{\rm exc}$ (grey shade) for the Rydberg atom to be excited, it then remains in the BEC for a time $t_{\rm imp}$ (green shade) and disappears at the beginning of the field ionization pulse of duration $t_{\rm ion}$ (red shade). We encode this in the function $\eta(t)$ (blue line), discussed in section 2.1, which parametrises presence or absence of a Rydberg atom. (c) We compare three different levels of detail for the calculation of the interaction potential between Rydberg and ground-state atoms. (i) The s-wave interaction potential $V_{\rm ryd,S}$ (black line) between the condensate and Rydberg impurity, with the nucleus of the latter at $x = 0$. (ii) The CASW $V_{\rm c}$ (blue lines), based on the classical electron probability distribution and (iii) the most complete s + p-wave potential $V_{\rm ryd,S+P}$ (red lines), which we cut off at $V_{\rm cut}$ (dotted purple lines). The radial axis is divided into two region (I and II) at $R_{\rm min}$ with a vertical green line, for the subsequent analysis. The S and S + P potentials agree for $\sqrt{r} \geqslant 0.7\ \mu{\rm m}^{1/2}$. For the s + p-wave potential, we do not adiabatically follow the asymptotic s-state all the way to $r = 0$, due to the initial presence of perturbers at all r (see appendix B).

electron wavefunction $\psi(\mathbf{R})$:

$$V_{\rm ryd,S}(\mathbf{R},t) = \eta(t) V_0(\mathbf{R} - \mathbf{x}_{n(t)}))\,|\psi(\mathbf{R} - \mathbf{x}_{n(t)})|^2. \tag{1}$$

Here $\eta(t) = 1$ at times where a Rydberg impurity is present and $\eta(t) = 0$ otherwise, see figure 1(b). The shape of the potential is mainly set by the Rydberg electron density $|\psi(\mathbf{R})|^2$, where $\psi(\mathbf{R}) = \langle \mathbf{R}|\psi\rangle$, since the prefactor $V_0(\mathbf{R}) = 2\pi\hbar^2 a_{\rm s}[k(\mathbf{R})]/m_{\rm e}$ only weakly varies as a function of position through the energy dependence of the electron–atom s-wave scattering length $a_{\rm s}[k(\mathbf{R})]$. The energy dependent s-wave scattering length is obtained from the phase shift of the electron–atom scattering [25], with zero energy scattering length $a_{\rm s}[0] = -16.05 a_0$ [26]. For a given Rydberg electronic state, the electron–atom collision energy is given by $\hbar^2 k^2(\mathbf{R})/2m_e = E_{\nu^*} + e^2/(4\pi\epsilon_0 r)$, where $E_{\nu^*} = -R_{\rm Ryd}/\nu^{*2}$ is the electronic energy for the effective principal quantum number ν^* including quantum defects [27, 28]; $r = |\mathbf{R}|$, $R_{\rm Ryd}$ is the Rydberg constant and $m_{\rm e}$ is the mass of the electron.

The potential (1) takes only s−wave collisions between electron and BEC atoms into account, which is a valid approximation for a low energy electron, sufficiently far away from the core of Rydberg atom. However, due to a shape resonance for electron–^{87}Rb scattering in the $^3P^0$ channel at 0.02 eV [29], this approximation does not hold all the way to the core. To account for that the effective potential has to be extended by incorporating also higher partial waves [30]. The calculation and non-standard choice of the full interaction potential including p-wave scattering is discussed in appendix B. Essentially, we find energy surfaces $V_{\rm ryd,S+P}(\mathbf{R})$ from the eigenvalue equation (for the ion at the origin)

$$\hat{H}_{\rm el}(\mathbf{R})|\,\varphi(\mathbf{R})\rangle = V_{\rm ryd,S+P}(\mathbf{R})|\,\varphi(\mathbf{R})\rangle, \tag{2}$$

where $\hat{H}_{\rm el}(\mathbf{R})$ is the Hamiltonian for the Rydberg electron including a ground-state atom perturber at location $\mathbf{R}$, and the state $|\varphi\rangle$ is the one having the largest overlap with $|133s\rangle$ at large R, see reference [31]. This approximate potential is based on a picture of a single perturber and the Rydberg atom, for many perturbers in the Rydberg orbit we except it to require modifications close to the p-wave shape resonance, where the electron–atom interaction starts to significantly mix electronic orbitals. Elsewhere it ought to be additive, based on perturbation theory arguments.

The two potentials, with and without p-wave contribution, are shown in figure 1(c). While not visible in the plotted range of energies, the s + p-wave potential is vastly stronger at shorter R, reaching to $V \approx -680$ MHz. For numerical stability, we cut this divergence off when $V = V_{\rm cut}$. To ensure convergent results, we investigate the dependence on $V = V_{\rm cut}$. One of the objectives of this article is to explore to which extent the detailed shape of the interaction potential and cutoff affects the BEC response. Hence we will compare simulation results arising from both these potentials and varied cutoffs.

Also the highly oscillatory character that is inherited from the radial part of the Rydberg wavefunction poses numerical challenges. This can be partly alleviated by replacing the Rydberg-electron wavefunction with a classical approximation [32], as discussed in [15]. To this end, we consider a third potential, referred to as 'classical approximation of s-wave' (CASW), in which we replace (1) for ion at the origin by

$$V_{\rm c}(\mathbf{R},t) = \eta(t)V_0(\mathbf{R}) \begin{cases} \rho^{\rm Q}(\mathbf{R}) & r < R_{\rm min}/2, \\ \rho^{\rm cl}(\mathbf{R}) & R_{\rm min}/2 < r < R_{\rm ct}, \\ \rho^{\rm Q}(\mathbf{R}) & r \geqslant R_{\rm ct}, \end{cases} \tag{3}$$

where $\rho^{\rm Q}(\mathbf{R}) = |\psi(\mathbf{R})|^2$ and $\rho^{\rm cl}(\mathbf{R})$ (see appendix B) are the quantum and classical electron probability densities respectively, as used in reference [15], $R_{\rm ct}$ is the outer classical turning point and $R_{\rm min} \approx 0.1$ μm or $\approx 1900a_0$. The latter is the distance of the Rydberg nucleus from the shape resonance in electron–^{87}Rb scattering for the $|\nu l\rangle = |133s\rangle$ Rydberg state, as indicated in figure 1(c). The approximation (3) is sketched in figure 1(c) as a blue line. The rapid oscillations of s-wave and s + p-wave potentials are not all discernible on the scale of figure 1(c), hence we plotted potentials in an order such that each envelope can clearly be seen.

2.2. Temporal excitation sequence

The excitation sequence creating a single Rydberg impurity at a time, subsequently removing it by field ionization, and then repeating the cycle is sketched in figure 1(b). Here $t_{\rm exc}$, $t_{\rm imp}$, and $t_{\rm ion}$ are the times taken to excite the Rydberg state, free imprint time, during which the Rydberg atom resides in the BEC, and the time for ionization of the Rydberg impurity, respectively. Therefore, the time τ taken for $N_{\rm exc}$ repeated excitations to complete before the free evolution time ($t_{\rm imag}$) of the BEC is $\tau = N_{\rm exc}(t_{\rm exc} + t_{\rm imp} + t_{\rm ion})$.

In our simulations for $N_{\rm exc} > 1$, the location of the ionic core of the nth Rydberg atom $\mathbf{x}_{n(t)}$ is randomly drawn from a three-dimensional (3D) Gaussian distribution, with Cartesian standard deviations $\sigma_{x,y,z}$. For this we determined parameters $\sigma_{x,y,z}$ corresponding to a given excitation laser beam profile and background density profile in appendix A. Only for simulations with $N_{\rm exc} = 1$, the Rydberg location is at the origin. To model the sequence shown in figure 1, $\mathbf{x}_n(t)$ is thus a step-wise continuous vector function, assembled from the $N_{\rm exc}$ random 3D positions $\mathbf{x}_n$ and the integer index $n(t) = \lfloor t/\tau \rfloor$. Finally, $\eta(t)$ is given by $\eta(t) = \sum_{n=0}^{N_{\rm exc}-1} \bar{\eta}(t - n\tau)$, with $\bar{\eta}(t) = \left[\tanh(\frac{t-t_{\rm exc}}{\xi}) + \tanh(\frac{t_{\rm imp}-t}{\xi})\right]/2$, with near instantaneous risetime ξ.

2.3. Condensate response

In order to understand how the excitation sequence of Rydberg impurities affects the BEC, we model the latter using the Gross–Pitaevskii equation (GPE) and assume an immobile Rydberg atom, thus treating the impurity potential (1) as external potential [9, 14, 16, 33, 34]. The resulting GPE including the interaction with the Rydberg impurity is

$$\mathrm{i}\hbar\frac{\partial}{\partial t}\phi(\mathbf{R}) = \left(-\frac{\hbar^2}{2m}\nabla^2 + W(\mathbf{R}) + U_0|\phi(\mathbf{R})|^2 \ + V_{{\rm ryd,S},n}(\mathbf{R},t) + \mathrm{i}\hbar\frac{K_3}{2}|\phi(\mathbf{R})|^4\right)\phi(\mathbf{R}), \tag{4}$$

where $\phi(\mathbf{R})$ is the condensate wave-function, and $W(\mathbf{R}) = m(\omega_x^2x^2 + \omega_y^2y^2 + \omega_z^2z^2)/2$ is the 3D harmonic trap, using $\mathbf{R} = [x,y,z]^{\rm T}$. The strength of interactions among ground-state ^{87}Rb atoms in the condensate is set by $U_0 = 4\pi\hbar^2a_b/m$, where $a_b = 109a_0$ is the s-wave scattering length. The last term on the right-hand side of (4) phenomenologically incorporates short-range three-body loss of the BEC. We take a rate constant $K_3 = 1.8 \times 10^{-41}$ m^6 s^{-1} [35–38] assuming a hyperfine state $|F, m_F\rangle = |2,2\rangle$.

The complex-valued condensate wavefunction can be written as $\phi(\mathbf{R}) = \sqrt{\varrho}\,\mathrm{e}^{\mathrm{i}\varphi(\mathbf{R})}$, with real density $\varrho(\mathbf{R})$ and real phase $\varphi(\mathbf{R})$. In the Raman–Nath approximation, the initial effect of the Rydberg impurity is

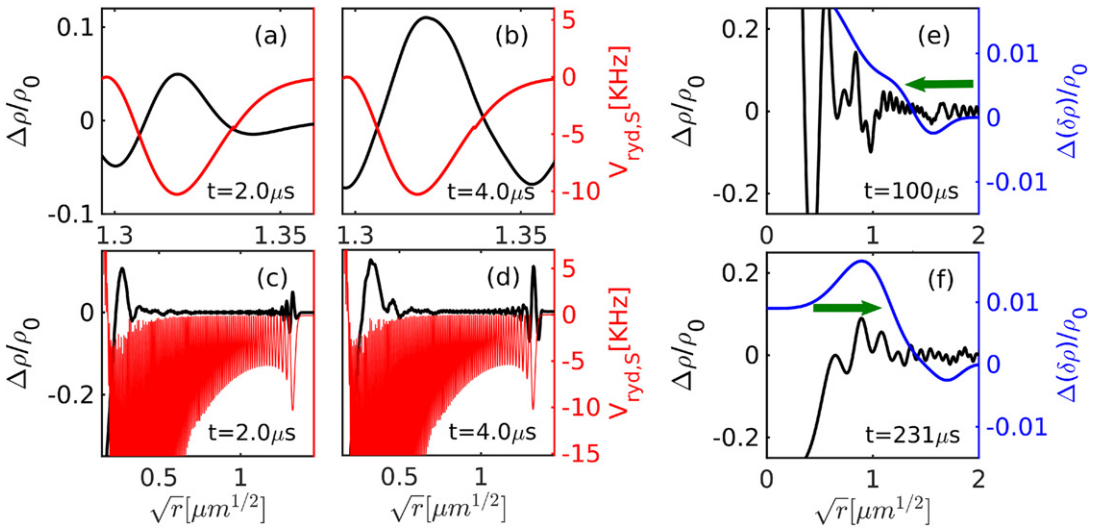

Figure 2. Condensate response to a Rydberg impurity in the spherically symmetric case. The left y-axis shows the condensate density relative to the background density $\rho_0 = 400\ \mu\text{m}^{-3}$, i.e. $\Delta\rho/\rho_0 = (\rho - \rho_0)/\rho_0$, and the s-wave interaction potential in equation (1) is shown on the right y-axis of panels (a)–(d). (a) The condensate density (black solid line) at the imprint time $t_{\text{exc}} + t_{\text{imp}} = 2.0\ \mu$s in the outer radial well (red line). (b) The condensate density in the outer well before ionizing the Rydberg impurity at $t_{\text{exc}} + t_{\text{imp}} = 4.0\ \mu$s. The density over the whole range of radii is shown in (c) and (d) in the same style as for panels (a) and (b), respectively. The density at late time after some evolution with impurity removed is shown at $\tau + t_{\text{imag}} = 100\ \mu$s in (e) and $\tau + t_{\text{imag}} = 231\ \mu$s in (f) as black line. In (e) and (f) the solid blue line using the right axis is a radial cut through the 3D spatially smoothened density, using a Gaussian kernel with a standard deviation of $\sigma = 0.5\ \mu$m; note the different y-axis scale. The green arrow in (e) and (f) indicates the inward and outward flow of the condensate, respectively.

then to imprint a phase $\varphi(\mathbf{R}) = -V_{\text{ryd}}(\mathbf{R})\Delta t/\hbar$ within a short time Δt [14, 39] while leaving the density relatively unaffected. Only with some delay will phase gradients, corresponding to initially imparted momentum, be converted into variations of condensate density through motion of the ground-state atoms [15]. For a numerically and conceptually tractable model, we ignore the backaction on the Rydberg impurity in the present study.

3. Condensate response in the mean field

3.1. Single spherical excitation

We first consider the case of a single impurity excited to the $|\nu l\rangle = |133s\rangle$ Rydberg state at $[x, y, z]^{\text{T}} = [0, 0, 0]^{\text{T}}$ in a homogeneous BEC of density $\rho_0 = 4.0 \times 10^{14}\ \text{cm}^{-3}$. All our results also in later sections pertain to this density. Due to the spherical symmetry of the Rydberg s-state, the entire problem is spherically symmetric, and we can solve the radial GPE instead of (4), which using $\phi(\mathbf{R}) = u(r)/r$ for $r = |\mathbf{R}|$ becomes [37]

$$\text{i}\hbar\frac{\partial}{\partial t}u(r,t) = -\frac{\hbar^2}{2m}\frac{\partial^2 u(r,t)}{\partial r^2} + \frac{U_0}{r^2}|u(r,t)|^2 u(r,t) \ + V_{\text{ryd,S},n}(r)u(r,t), \tag{5}$$

where $u(r)$ is a radial condensate wavefunction, normalised such that $\int_0^\infty \text{d}r|u(r)|^2 = N$. We discuss in appendix C how to handle the practical implementation in a homogenous system using the fast-Fourier-transform (FFT) for derivatives. Equation (5) is finally solved using the high level computing language XMDS [40, 41], which invokes an adaptive step-size 8/9th order Runge–Kutta method [42] for time-stepping, and the FFT for calculating the Laplacian.

For now, we do not yet consider three-body loss ($K_3 = 0$) and allow the Rydberg impurity to interact with the condensate through the s-wave interaction potential (1). We show the resulting dynamics of the condensate density deviation from the background density $\Delta\rho = \rho(r) - \rho_0$ in figure 2 as function of $\sqrt{r}$. The condensate particles respond to each radial well of the s-wave interaction potential initially, accelerating towards its center, shown for the outermost well in the range $1.3\ \mu\text{m}^{1/2} < \sqrt{r} < 1.35\ \mu\text{m}^{1/2}$ at $t_{\text{exc}} + t_{\text{imp}} = 2.0\ \mu$s in panel (a) of figure 2, where $t_{\text{exc}} = 0.5\ \mu$s and $t_{\text{imp}} = 1.5\ \mu$s. These intervals were chosen to ensure continued existence of the Rydberg state in that time, which has an effective lifetime of a few μs in the medium [22]. While the relative density contrast near the outer well increased by a factor of about three within an additional imprint time $\Delta t = 2.0\ \mu$s towards panel (b), as long as the Rydberg impurity remains present, the maximal relative density increase reaches only 13% in the outer well.

In figures 2(c) and (d), we show the density in the full radial range at the same times as in (a) and (b). While the condensate response to the outer well of the impurity potential is significant, the response to most of the inner wells remains disproportionally small. We can understand this from the fact that the healing length here is $\xi = 1/(2\sqrt{2\pi a_b \rho_0}) = 0.13\ \mu$m for Rb s-wave scattering length $a_s = 109a_0$, hence only the outer well is wider than this scale. The response to all other wells would be fast due to their tightness, but is suppressed by the inability of the mean field to respond on that length scale. This will also be true for other atomic species and different realistic combinations of densities and principal quantum numbers, since densities for which the healing length becomes less than any of the middle wells are so extreme that inelastic processes would significantly affect the BEC and the Rydberg atom [22]. Altogether, the net effect on the density remains small at the imprint time ($t_{\rm exc} + t_{\rm imp} = 4.0\ \mu$s), corresponding to the Raman–Nath regime [43]. In contrast, on larger time-scales the initial momentum imparted by the Rydberg impurity keeps the condensate flowing towards the origin, leading to a much increased relative density there. We find $\Delta\rho/\rho_0 \approx 2.5$ near the ionic core at $\tau + t_{\rm imag} = 100\ \mu$s for the case of figure 2(e), where $\tau = t_{\rm exc} + t_{\rm imp} + t_{\rm ion} = 4.8\ \mu$s is the time taken to complete one excitation and its subsequent removal ($t_{\rm ion} = 0.8\ \mu$s) as discussed in section 2.2.

In figure 2(e), we show the spatially smoothened density $\delta\rho$ as a blue line, to demonstrate the net inwards flow towards the Rydberg ion. We obtain the latter as the spatial average of the 3D condensate density over a Gaussian kernel, $\delta\rho(\mathbf{R}) = \mathcal{N}\int \mathrm{d}^3\mathbf{R}'\ \exp(-2(|\mathbf{R}-\mathbf{R}'|^2/\sigma^2))|\phi(\mathbf{R}')|^2$, with a standard deviation of $\sigma = 0.5\ \mu$m and normalization constant $\mathcal{N}$. For this task, we solve the 3D GPE (4) using $512 \times 512 \times 512$ grid points and accepting a slightly undersampled Rydberg potential. Through comparison of the 3D simulations with undersampled potential and radial 1D simulations with resolved potential, we ensure that all qualitative conclusions presented here are consistent in both simulations.

After piling up in the centre, the excess condensate density then subsequently reduces again as atoms keep moving with their inertia, resulting in an outward flow of condensate particles at later times, see figure 2(f). Overall we see that the initial net impact of the excitation is to contract the BEC towards its location, which seems intuitive given the net attractive character of the s-wave potential in figure 1(c), when spatially averaged over all the wells. The condensate dynamics described is qualitatively unchanged also at other principal quantum numbers for the present density (not shown).

3.2. Dependence on potential details

There are two main features of the potentials in figure 1(c) that can be considered at varying levels of approximation:

(i) The rapid oscillations stemming from the radial Rydberg wavefunction could be removed when replacing the potential with the CASW variant (3), while leaving the net attractive character intact. This replacement can help to keep numerical simulations of larger condensates tractable. Since the characteristic length scale for mean-field condensate dynamics is given by the healing length $\xi = 0.13\ \mu$m, which is much larger than the radial oscillation wavelength of the exact potential, one can except the effect of those oscillations to be somewhat averaged out, as we confirmed in section 3.1.

(ii) While the s-wave and the s + p-wave potentials agree for $r > R_{\rm min}$, they deviate significantly closer to the nucleus. However, in three dimensions, the corresponding volume is a small fraction of the Rydberg orbital volume (5% at $n = 133$), and hence the importance of this difference for the BEC dynamics at larger distances from the nucleus is not a priory clear.

To understand if and on what length-scales points (i) and (ii) make a difference, we compare the BEC dynamics for all three potentials in figure 3. For guidance, we divide the radial range into two regions, defining an inner (I: $0 \leqslant r < R_{\rm min}$), and an outer (II: $r \geqslant R_{\rm min}$) region as indicated by the solid vertical green line as shown in figure 3. As evident from panel (a) the impact on the condensate is the same in the inner region for the s-wave and CASW potentials because these two potentials are near identical in this range, while in the outer region the s-wave response matches with that due to the s + p-wave interaction potential since here these other two potentials largely agree. In comparison to the s-wave potential and CASW, the s + p-wave potential causes a much stronger perturbation in the condensate density at the end of the imprint time, leading a relative increase of $\Delta\rho/\rho_0 \approx 10$ at the location of the ionic core. This is due the presence of the shape-resonance which provides a large central peak $V \approx -680$ MHz, see figure 1(c), which was cut at $|V_{\rm cut}| = 1$ MHz for the simulations in figure 3. Even when cutting off the s + p potential, it remains much stronger than that using only the s-wave approximation in the central region.

As can be seen in figure 3(b), for all three potentials the initial inward motion of the condensate is converted to an outward flow due to inertia at later times after the Rydberg impurity was removed, as discussed in section 3.1. The wave created by the s + p-wave potential at $\tau + t_{\rm imag} = 15.0\ \mu$s has reached the outer region and still has an about five times larger amplitude than that generated by the other two

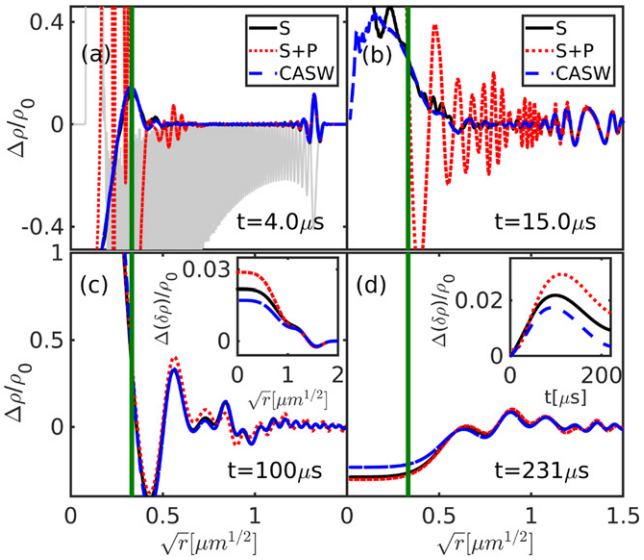

Figure 3. Motion of the BEC in different approximations of the Rydberg interaction potentials. The condensate density is shown relative to the background density as in figure 2. (a) Atom density in interaction potentials, s-wave (solid black line) equation (1), s + p-wave (dotted red line) equation (2), and CASW (dashed blue line) equation (3) are shown at the imprint time $t_{\rm exc} + t_{\rm imp} = 4.0\ \mu$s. The s-wave potential for the $|\nu l\rangle = |133s\rangle$ state is indicated without scale as grey lines for guidance. Green vertical lines divide the radial coordinate into an inner region (I: $0 \leqslant r < R_{\rm min}$) and an outer region (II: $r \geqslant R_{\rm min}$). (b) The large density perturbations caused by the shape-resonance using the s + p-wave potential becomes more prominent in the outer region at times $\tau + t_{\rm imag} = 15.0\ \mu$s, after the ionization of the Rydberg impurity. Further snap shots of the density after free evolution are shown in (c) and (d) at $\tau + t_{\rm imag} = 100\ \mu$s and $\tau + t_{\rm imag} = 231\ \mu$s respectively. The inset of (c) shows the spatially averaged 3D density at $\tau + t_{\rm imag} = 100\ \mu$s. The inset of (d) shows the variation of the averaged density over time at the Rydberg ion location ($x = y = z = 0$). For further details see the supplementary movie (https://stacks.iop.org/NJP/24/073005/mmedia).

potentials. Therefore, a signature of the shape resonance should be accessible through very high resolution *in situ* density measurements [44, 45] or electron microscopy [46]. While the density waves created near the position where the Rydberg core has been removed depend on the level of detail used in the potential, we see that at much later times and larger radii, the waves created by all three potentials nearly agree. This shows that this part of the wave dynamics is not too sensitive to either fast oscillations or deviations between s-wave and s + p-wave potential in the inner region, see figures 3(c) and (d). We do, however, find that the smoothened relative density perturbations $\Delta(\delta\rho)$ caused by the s + p-wave potential remain approximately 1.5 times (2 times) larger than those due to the s-wave potential (CASW potential), in the region $r < 1\ \mu$m at $\tau + t_{\rm imag} = 100\ \mu$s (see the inset of panel (c)). Moreover, when directly comparing the average density due to the s-wave and CASW potential in the inset of the panel (c), one finds that the average maximum density ($\delta\rho$) with the s-wave potential is about 1.5 times higher than from the CASW potential in the region $r < 1\ \mu$m at $\tau + t_{\rm imag} = 100\ \mu$s. Thus, further out, the radial wells in the potentials play a slight quantitative but not a qualitative role in the Rydberg-BEC dynamics. In all cases atoms are first focussed inwards and only then diffuse outwards, as discussed in section 3.1. This results in the non-monotonic behaviour of the central density at the ionic core, visible in the inset of figure 3(d).

An important conclusion that we can already draw from this present analysis is that the net condensate perturbation at large R and late times t is qualitatively insensitive to either of the details (i) and (ii) defined above. Both features are characterised by length scales much smaller than the healing length of $\xi = 0.13\ \mu$m, so that the condensate will only respond according to an averaged effect. This spatial averaging will make the impact of details even less prominent when the impurity is moving, as we have shown in [15]. Insensitivity of the condensate response to the detailed inner potential is a particularly important discovery, given that the true potential for a many-body scenario is not known there. Note, that the short-range ion-atom polarization potential does not significantly affect the condensate dynamics on the length scales relevant here, hence we did not explicitly include it in our discussion.

3.3. Dependence on numerical potential cutoff $V_{\rm cut}$

While the s + p-wave potential agrees with the s-wave potential in the outer region, they significantly deviate close to the nucleus where the former reaches down to $V = -680$ MHz. This poses severe challenges for a wide range of schemes used to numerically propagate the 3D GPE, for which the potential drop enforces very small time steps. Here we thus separately analyse the importance of a complete inclusion of the potential step, using the radial GPE (5), cutting the central potential peak at $V = -V_{\rm cut}$, as shown in

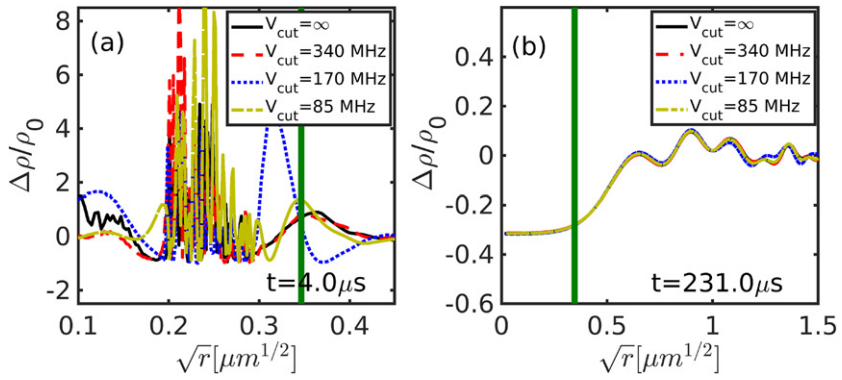

Figure 4. Dependence of atom dynamics on potential cutoffs. (a) Relative condensate density variation $\Delta\rho = \rho - \rho_0$ for $\rho_0 = 400\ \mu\text{m}^{-3}$ in the inner region at the imprinting time $t_{\text{exc}} + t_{\text{imp}} = 4.0\ \mu$s. We use $V_{\text{cut}} = \infty$ (no cut-off, solid black lines), $V_{\text{cut}} = 340$ MHz (dotted red lines), $V_{\text{cut}} = 170$ MHz (dashed blue lines) and $V_{\text{cut}} = 85$ MHz (dot-dash yellow-sh lines). The resulting dynamics after removing the Rydberg atom, at later times and larger radii, is shown in (b), for $\tau + t_{\text{imag}} = 231.0\ \mu$s. The solid green line at $r = R_{\text{min}}$ divides the potentials into two regions at the shape resonance.

figure 1(c), and then varying V_{cut}. Since the condensate response for the outer region at the imprint time $t_{\text{exc}} + t_{\text{imp}} = 4.0\ \mu$s will obviously still be the same for different cutoff values, we only show the zoom onto the inner region in figure 4(a).

As expected, the density perturbations of the condensate in the inner region significantly depend on V_{cut}. However, counterintuitively, the amplitude of the perturbations does not follow a monotonic trend with V_{cut}. For the snapshot shown, the oscillations are largest for $V_{\text{cut}} = 85$ and 340 MHz while they are significantly smaller for 160 MHz and ∞ (no cutoff) in the region $0.2\ \mu\text{m}^{1/2} < \sqrt{r} < 0.3\ \mu\text{m}^{1/2}$. Relative amplitudes then vary in time. However, while the initial density fluctuations in the inner region of the potential depend strongly on the magnitude of V_{cut}, we find that the late time dynamics of the condensate becomes nearly cut-off independent, see figure 4(b).

We can thus conclude that the huge central dip of the s + p-wave does not contribute significantly to the overall late time dynamics of the BEC. Therefore, we fix the cut-off at $|V_{\text{cut}}| = 2$ MHz for further investigation in the coming sections.

3.4. Repeated excitation

In section 3.1 we found that a single Rydberg excitation only causes a minor relative change (a maximum of about 1%) of the atom density on percent level at $\tau + t_{\text{imag}} = 260\ \mu$s. As a consequence, experiments will likely require repeated excitations to measurably affect the bulk density. First steps in this direction have been recently taken in reference [9]. Here, we model a sequence of $N_{\text{exc}} = 10$ repeated excitations with a probabilistic approach. In contrast to the case of single excitation, the Rydberg atoms are no longer located at the origin, but have random positions with a Gaussian distribution using standard deviations $\sigma_x = 1.0\ \mu$m, $\sigma_y = 2.0\ \mu$m, and $\sigma_z = 1.0\ \mu$m respectively. This assumes a relatively tight excitation laser focus as sketched in figure 1(a). We have modelled a specific excitation scenario to obtain the spatial widths that we describe in appendix A. The uncertainty in excitation location breaks spherical symmetry, so that we have now to turn the full solutions of the 3D GPE (4). For the temporal sequence we use an excitation duration of $t_{\text{exc}} = 0.5\ \mu$s, imprint time $t_{\text{imp}} = 3.5\ \mu$s and ionization time of $t_{\text{ion}} = 0.8\ \mu$s. Thus N_{exc} repeated excitations will require a total time $N_{\text{exc}} \times 4.8\ \mu$s.

Since we are starting from an already quite dense condensate with $\rho_0 = 4 \times 10^{14}\ \text{cm}^{-3}$, and find a large increase in condensate density around the core of the Rydberg atom during the time evolution see, e.g., figure 3, it is conceivable that three-body losses might become relevant. To investigate this, we have include the three-body loss term in the simulations for this section, and compare the total loss of atoms with and without Rydberg excitation. While 500 atoms are lost out of a total of 6.7×10^5 atoms in our simulation volume, the difference between those two scenarios is negligible. Hence we conclude that Rydberg excitations do not significantly increase atom losses. This implies that the overdense region are too small to induce strongly enhanced three-body losses.

We show the results after $N_{\text{exc}} = 10$ excitations in figure 5(a), using the s + p-wave interaction potential (2). The figure shows 2D slices of the 3D density at $z = 0$, as well as column densities $\rho_c = \int \text{d}z\, \rho(\mathbf{R})$. Each circular feature is due to one Rydberg excitation, see supplementary movie. In contrast to the case of a single Rydberg atom in the BEC, right after the excitation a significant accumulated impact ($\Delta(\delta\rho)/\rho_0 \approx 1\%$) can be seen in the smoothened condensate column density after 10 repeated excitations

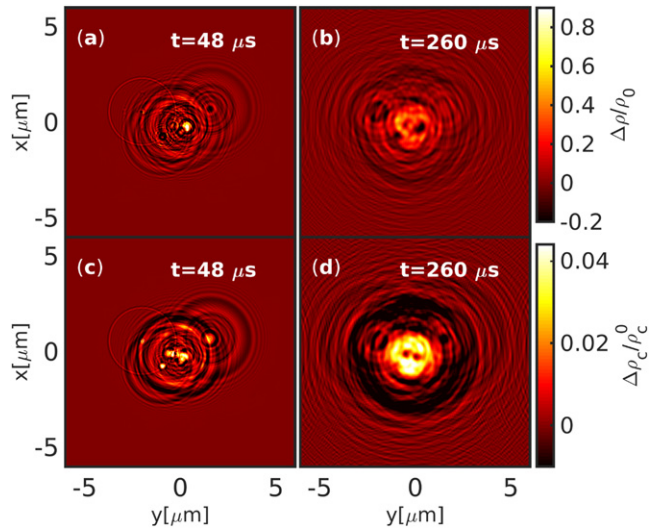

Figure 5. Relative condensate density after repeated excitations of Rydberg impurities. (a) The 2D slice of the 3D density at $z = 0$ after $N_{\rm exc} = 10$ repeated excitations at $t = \tau' = 10 \times 4.8 = 48$ μs. The radius of circular features is that of the Rydberg orbit, which is about 1.8 μm for $|\nu l\rangle = |133S\rangle$. The subsequent time evolution of the density is shown in (b) at $t = \tau' + t_{\rm imag} = 260$ μs. The relative column density under the same conditions as in (a) and (b) is shown in (c) and (d). See also supplementary movie.

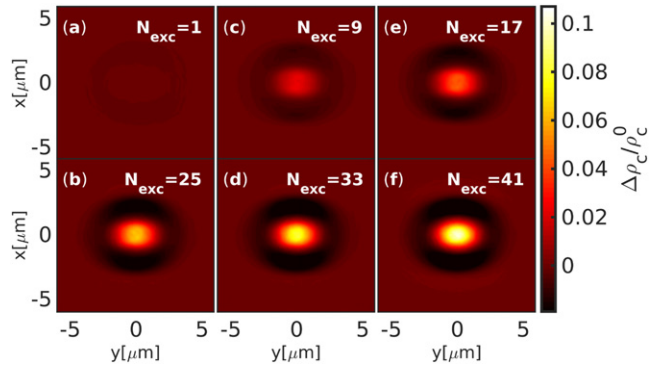

Figure 6. Signals using $N_{\rm exc}$ repeated Rydberg excitations. The column density relative to the background column density $\rho_{\rm c}^0 = 4.76 \times 10^3$ μm^{-2}, i.e. $\Delta\rho_{\rm c} = \rho_{\rm c} - \rho_{\rm c}^0$ is shown here. (a) Column density for a single Rydberg excitation ($N_{\rm exc} = 1$) at $\tau + t_{\rm imag} = 260$ μs, averaged over 400 samples of Rydberg positions. As the number of repeated excitations is increased from $N_{\rm exc} = 1$ to $N_{\rm exc} = 41$, the features in the column density become more pronounced, from (a) to (f).

are completed. The impact becomes even more evident after an additional evolution time of $\tau' + t_{\rm imag} = 260$ μs as shown in figure 5(b), where $\tau' = 10 \times (t_{\rm exc} + t_{\rm imp} + t_{\rm ion}) = 48$ μs is the time taken to complete 10 repeated excitations with the subsequent removal of the Rydberg excitation.

While Rydberg excitations leave a visible mark in both densities a detailed inspection of the contrast between maximum and minimum, reveals a higher maximal contrast in the 3D density (8% of the mean) than the column density (1% of the mean), even though the simulation box is only extended over $L_z = 6$ μm in the z-direction. As part of a larger cloud, the column density signal would be even weaker. Nonetheless, for the case here, the signal appears prominent over a larger spatial region in the column density, leaving a clear density depression of 1.2% in panel (d) around the central enhancement of the density. The latter is due to the constructive interference of waves directed towards the centre by each of the excitations, as discussed in section 3.1.

An experimental density measurement might additionally involve an averaging over $N_{\rm samp}$ repeated measurement. We explore how the expected density profile depends on the number $N_{\rm exc}$ of repeated excitations in figure 6. The figure shows the averaged column density at $t = 4.8 \times N_{\rm exc} + t_{\rm imag} = 260$ μs, subtracted from the background column density at $t = 0$, and averaged over $N_{\rm samp} = 400$ samples, each with a different random realisation of the Rydberg atom positions. We show each snapshot at the same time t, hence the delay $t_{\rm imag}$ between the last excitation and the snapshot shown is varying as $t_{\rm imag} = (260 - 4.8 \times N_{\rm exc})$ μs. We clearly see that by increasing the number of excitations from $N_{\rm exc} = 1$ to

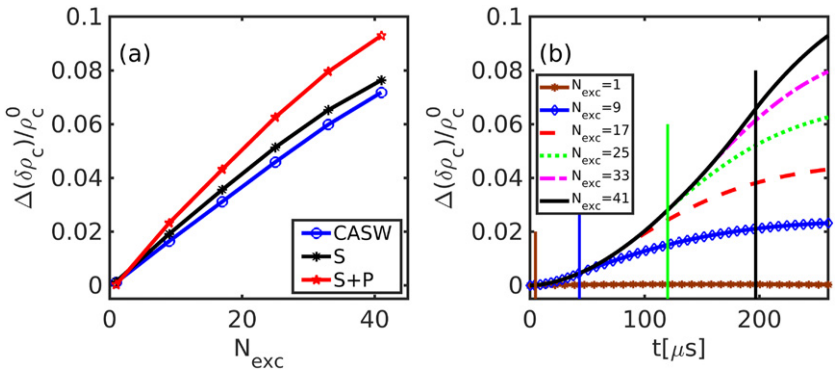

Figure 7. Increase in the smoothened relative column density at the ion location ($x = y = 0$) for different repeated excitations comparing in (a) the s-wave potential (1) (black solid and $*$), CASW potential (3) (blue solid and $\circ$) and the s + p-wave potential (2) (red solid and $\star$), at a fixed time $t = N_{\rm exc} \times 4.8\ \mu{\rm s} + t_{\rm imag} = 260\ \mu{\rm s}$. (b) Evolution of the smoothened column density for different numbers of repeated excitations at $x = y = 0$, considering the s + p-wave interaction potential. Smoothing uses a Gaussian kernel with a standard deviation of $\sigma = 0.5\ \mu$m in both panels. Vertical coloured lines indicate at what time a given number of excitations $N_{\rm exc}$ is complete.

$N_{\rm exc} = 40$, the relative density contrast of the resultant feature improves from about 0.1% to near 11%. As before, we see that the net effect is a central density increase, surrounded by a density depression. The feature should be visible through *in situ* density measurements [44–46]. The late-time dynamics of the condensate follows the same qualitative trend for all different interaction potentials, with a moderate quantitative difference at the central location, as shown in the inset of figure 3(c). We map this difference at $x = y = 0$ in more detail through multiple repeat excitations, with results shown in figure 7(a), averaged over $N_{\rm samp} = 400$ samples. The data clearly follows the same pattern for all three potentials, but with slightly different slopes. While the full s + p-wave potential creates the largest density increase, a difference is still visible between the signature generated by the s-wave and CASW potentials, which again suggests that the radial wells do not qualitatively change the picture but have a discernible quantitative effect.

Note, that we have restricted our simulation to $128 \times 128 \times 128$ grid points which allowed us to afford the average over $N_{\rm samp} = 400$ position realisation. Based on our findings in section 3.1, we expect this to undersample the interaction potential, but not lead to a qualitatively modified condensate dynamics. Nonetheless, the net density contrast for the s-wave and s + p-wave potentials will increase by up to a factor of two for more grid points $512 \times 512 \times 512$. Therefore, due to computational constraints, we report a lower bound on the density perturbation caused by repeated excitations.

Finally, in figure 7(b) we show the increase in time of the signal contrast, for different numbers of excitation $N_{\rm exc}$. We can see that the largest contrast that is reached at late times scales roughly linear with $N_{\rm exc}$, while the earliest time for which a given fixed contrast is reached no longer reduces with $N_{\rm exc}$ after a certain number of excitations. For example, a contrast of 2% is reached at $t \approx 100\ \mu$s in figure 7, for all $N_{\rm exc} \geqslant 17$ regardless of $N_{\rm exc}$. We see that for $N_{\rm exc} > 1$, an additional time of Rydberg-free evolution significantly enhances the signal, and thus might be an important experimental tool for a more visible effect.

4. Local heating of the condensate

It has been found previously that a Rydberg impurity excited in the BEC causes atom-loss and heating, increasing with the number of repeated excitations of a Rydberg impurity [9, 32]. In two-dimensions, we have shown in reference [15] that heating is limited when a small number of impurities is excited in a low density BEC background within the time span of a few microseconds. Specifically, the number of atoms entering the uncondensed fraction is not enough to invalidate the GPE. In this section we show that these conclusions remain unchanged for the scenarios considered in the work, i.e. in 3D and at higher densities. Importantly, we find that beyond mean field physics also do not significantly affect any of the earlier results discussed in this article. As we found that the three-body loss is negligible we do not consider its contribution in this section.

To study heating in the present context, we employ the truncated Wigner approximation (TWA) [47–53] which extends equation (4) (section 2.3) beyond mean-field theory. This is done by adding quantum and thermal fluctuations to the initial state through a specific recipe by the inclusion of random noise. The total atomic density $\rho_{\rm t}$ can then be split into the condensed density $\rho_{\rm c}$ and the uncondensed one

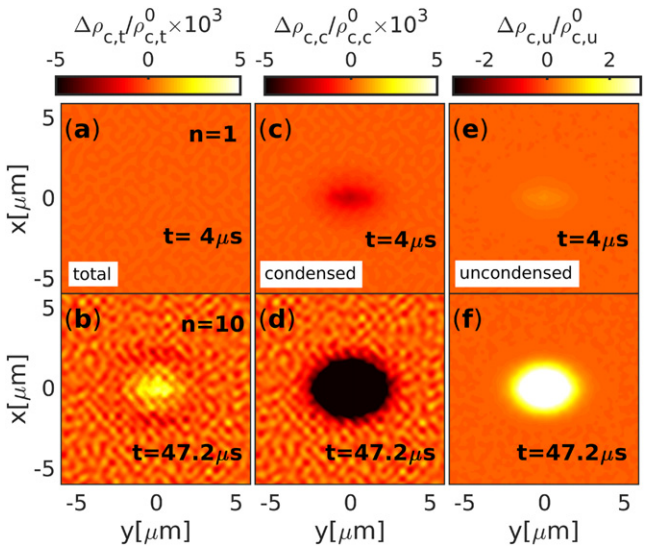

Figure 8. Beyond mean-field response of the Bose gas, using the s + p-wave potential (2), and averaging over $N_{\rm traj} = 5120$ trajectories for a single (top row) and ten (bottom row) excitations. The total relative column density, $\rho_{\rm c,t}$, for a single (a) and ten repeated excitations (b) at $t_{\rm exc} + t_{\rm imp} = 4.0\ \mu$s and $10 \times (t_{\rm exc} + t_{\rm imp}) + 9 \times t_{\rm ion} = 47.2\ \mu$s shows a weak impact of the Rydberg impurities within their respective imprint time, where $\rho^0_{\rm c,t} = 4.7 \times 10^3\ \mu{\rm m}^{-3}$ is the initial total column density. A clearer local signal can be seen in the condensed (d) and uncondensed components (f) of the BEC for ten repeated excitations, and a faint signal for the single excitation in the condensed (c) and uncondensed component (e), where $\rho^0_{\rm c,c} = 4.72 \times 10^3\ \mu{\rm m}^{-3}$ and $\rho^0_{\rm c,u} = 2.61 \times 10^1\ \mu{\rm m}^{-3}$ are the initial condensed and uncondensed column densities. We use a homogeneous mean density of 400.0 $\mu{\rm m}^{-3}$.

$\rho_{\rm u}$, after averaging over an ensemble of $N_{\rm traj}$ realisations of the noisy simulations as discussed in appendix D. For a single excitation with s + p-wave interaction potential (2) and averaging over random impurity positions as in section 3.4, we find that until $t_{\rm exc} + t_{\rm imp} = 4.0\ \mu$s, while the Rydberg impurity is present, it causes only an additional ≈65 atoms to become uncondensed, compared to their initial number, out of a total of 6.7×10^5 atoms in our simulation box. Focussing exclusively on the Rydberg excitation volume, a sphere with radius 2 μm, the uncondensed number thus increases by about 50 out of 13 400 atoms, corresponding to 0.4%. When adopting the repeated excitation scheme described in section 2.2 under the conditions of figure 5 ($N_{\rm exc} = 10$), we find that about 800 atoms in the box, and roughly 750 (6%) of the atoms in the Rydberg excitation volume are depleted from the condensate, compared to the initial state, up to time $t = 10 \times (t_{\rm exc} + t_{\rm imp}) + 9 \times t_{\rm ion} = 47.2\ \mu$s. These results suggest that heating is not strong enough to significantly alter the results of our earlier mean-field simulations, as we indeed shall see shortly.

When moving from bulk-data such as uncondensed atom numbers to local data such as the uncondensed density $\rho_{\rm u}(\mathbf{x})$, we see that the condensate heating is restricted to within the excitation volume. This is demonstrated in figure 8, for the conditions of the single and ten repeated excitations.

The first row contains the relative change of the total column density, $\rho_{\rm c,t}$, condensed column density, $\rho_{\rm c,c}$ and uncondensed column density $\rho_{\rm c,u}$ after a completed single excitation, at $t_{\rm exc} + t_{\rm imp} = 4.0\ \mu$s. The components are extracted from the stochastic field as described in appendix D. The second row shows snapshots after $N_{\rm exc} = 10$ repeated excitations at $t = 10 \times (t_{\rm exc} + t_{\rm imp}) + 9 \times t_{\rm ion} = 47.2\ \mu$s. It is evident from the uncondensed density in panel (e) that heating remains confined to within sphere with radius of 2 μm around $x = y = 0$ for a single excitation. This in turn leaves a hole of relative depth of about 0.2% in the same region of the condensed column density, see figure 8(c). However, since overall no atoms are lost, no features are caused at this time in the total density shown in figure 8(a). The depth of the dip in the condensed density increases by about 6.0% as one moves from a single to ten repeated excitations, as shown in figure 8(d). This happens since more atoms transfer to the uncondensed component for ten repeated excitations in comparison to a single excitation. Comparing the condensate density from TWA as shown in figure 8(d), see also appendix D, with the condensate density using the GPE (not shown) we find a qualitatively different behaviour as expected, since the GPE cannot describe local heating. Note, however, that experiments would only measure the total density as shown in figure 8(b) that appears similar to the mean field result.

We can see in figure 8(b) that a faint signature is visible already after $N_{\rm exc} = 10$ repeated excitations in the total density directly after the excitation period, despite the added noise due to residual fluctuations in the mean. The contrast is, however, comparable to the one in the mean-field scenario shown in figure 5(c), with the difference originating in the different number of realisations in the simulation. By waiting an

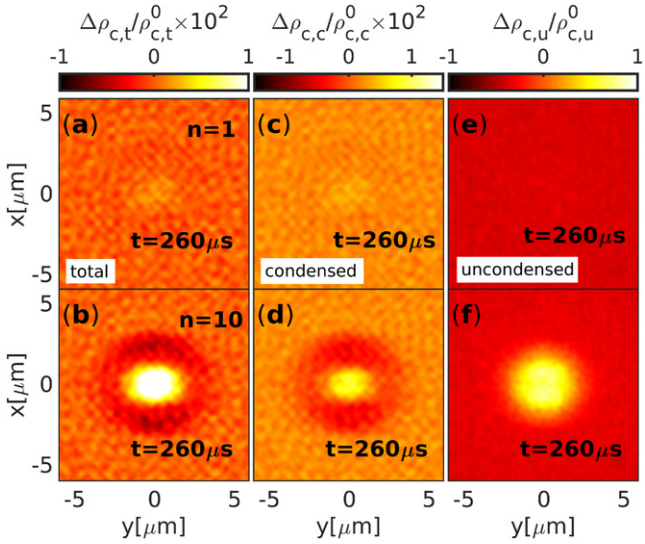

Figure 9. Evolution of the Bose gas following the Rydberg excitation beyond mean-field theory, for the same parameters as in figure 8. (a) and (b) The total column density for a single and ten repeated excitations at $t = \tau + t_{\rm imag} = 260.0\ \mu$s and $t = \tau' + t_{\rm imag} = 260\ \mu$s respectively shows a significant impact of the Rydberg impurities. We also show the condensed column density after a single excitation (c) and after ten repeated excitations (d), as well as the uncondensed column density after a single excitation (e) and after ten repeated excitations (f). Note the different colorscale compared to figure 8.

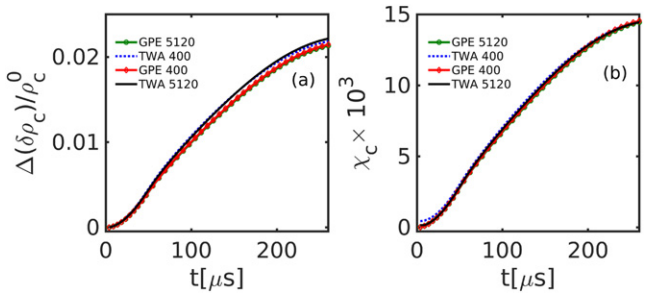

Figure 10. The column density averaged over a Gaussian kernel with width $\sigma = 1\ \mu$m is compared in (a) at the Rydberg core between mean-field simulations for $N_{\rm traj} = 5120$ (solid green and o) and $N_{\rm traj} = 400$ (solid red and ♢) and TWA simulations for $N_{\rm traj} = 5120$ (solid black lines) and $N_{\rm traj} = 400$ (dotted blue lines). The contrast (6) of the same quantities is shown in (b). We use ten repeated excitations, as in figure 8. The initial background column density for both simulations is $\rho^0_c = 4.76\times10^3\ \mu{\rm m}^{-2}$.

additional time the signal to noise ratio can be further enhanced, as suggested by figure 7(b). We show this explicitly in figure 9(b) after a free time evolution of $t = \tau' + t_{\rm imag} = 260\ \mu$s. The detailed time evolution of the local heating dynamics for single and ten repeated excitations is shown in the last two column of figure 9, indicating significant motional dynamics also in the uncondensed component at later times. If we now compare the late-time condensate density in TWA, figure 9(d), with the corresponding one using the GPE, figure 6(c) shows that these largely agree, as expected based on our earlier observation that only a small fraction of atoms becomes uncondensed and hence BEC bulk dynamics should be well described by the GPE simulations.

For a more quantitative comparison between TWA and GPE, we define the image contrast χ_c as the difference between the maximum and minimum in the smoothened relative column density according to

$$\chi_c = \frac{1}{2}\left[\left(\frac{\Delta(\delta\rho_c)}{\rho^0_c}\right)_{\rm max} - \left(\frac{\Delta(\delta\rho_c)}{\rho^0_c}\right)_{\rm min}\right], \tag{6}$$

where $\delta\rho_c$ is the smoothened column density, and $\Delta\delta\rho_c$ thus $\delta\rho_c - \rho^0_c$. In figure 10 we compare the time evolution of χ_c obtained from GPE simulations averaged over $N_{\rm traj}$ different realisations of atomic positions, with TWA simulations of $N_{\rm traj}$ trajectories. The latter combines two different averages: in each trajectory the atomic positions as well as the quantum noise realisation are different. The figure then compares $N_{\rm traj} = 400$ and 5120 trajectories. For better comparability, all column densities are first smoothened with a Gaussian kernel of resolution 1.0 μm.

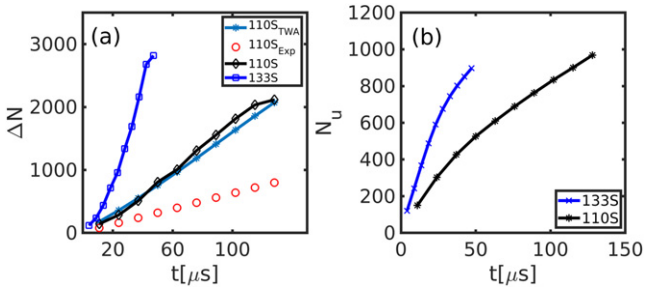

Figure 11. Number of atoms accelerated to high-momenta and uncondensed atom number calculated for a homogeneous BEC. (a) The high-momentum atom number $\Delta N(t)$ from a mean-field simulation for the Rydberg impurity in the Rydberg state $|110S\rangle$ at density $\rho = 100\ \mu\text{m}^{-3}$ (solid black lines with $\diamond$) and the total atom number in those modes from TWA (blue solid line with $*$) is compared with corresponding data from the experiment [9] (red $\circ$). The total time required to finish the ten excitations is $\tau = 10 \times (t_{\text{exc}} + t_{\text{imp}} + t_{\text{ion}}) = 130\ \mu\text{s}$. For orientation we show the same data for parameters used elsewhere in this work, using a Rydberg state $|133S\rangle$ and density $\rho = 400\ \mu\text{m}^{-3}$ (blue solid lines wit). Here the last excitation is finished at a time $\tau = 10 \times (t_{\text{exc}} + t_{\text{imp}} + t_{\text{ion}}) = 48\ \mu\text{s}$. (b) The uncondensed atom number calculated using TWA simulations for Rydberg state $|110S\rangle$ (black solid line with *) and $|133S\rangle$ (blue solid $\times$ lines) for the same regimes as in (a). The simulation is averaged also over $N_{\text{traj}} = 2560$ trajectories for $32 \times 32 \times 32$ Bogoliubov modes, which results in 0.5% standard error on mean 3D densities. Near all of these are above the momentum cutoff.

We see that the difference between TWA and GPE is very small when averaging over the same number of impurity positions, as expected from our earlier observation of only a minor impact of condensate heating. Increasing the sample size maintains the maximum contrast but results in a smoother image. Since this applies for the GPE simulations as well, we conclude that the average over all spatial realisations is converged at the chosen number of trajectories N_{traj}. For our 3D TWA calculations of a single and ten repeated excitations, we employed $128 \times 128 \times 128$ spatial grid-points and averaged over $N_{\text{traj}} = 5120$ trajectories, which results in about 0.5% standard error on mean 3D densities.

4.1. Comparison with experiments and atom loss versus heating

We can compare our simulations with measurements of atoms lost from the BEC due to Rydberg excitation therein, reported in [9]. For this we change parameters, only for this section, to a Rydberg state $|\nu l\rangle = |110S\rangle$, density $\rho_0 = 100\ \mu\text{m}^{-3}$ and pulse sequence $t_{\text{exc}} = 1\ \mu\text{s}$, $t_{\text{imp}} = 5\ \mu\text{s}$, and $t_{\text{ion}} = 7\ \mu\text{s}$ for excitation, imprint, and ionization intervals, respectively. Atom loss in [9] was measured by a reduction of the total atom number imaged in a predefined rectangular region after time-of-flight, which can be translated into atoms being accelerated above a certain momentum cutoff $|q_x|/\hbar, |q_y|/\hbar > q_{\text{cut}}/\hbar = 5.0 \times 10^5\ \text{m}^{-1}$ prior to time-of-flight [54]. We use no cutoff along the imaging direction (q_z). For mean-field calculations based on (4) we define the number of lost atoms as $\Delta N(t) = \int \text{d}^3\mathbf{q}_{|q_x|,|q_y|>q_{\text{cut}}} |\tilde{\phi}(\mathbf{q}, t)|^2$, where $\tilde{\phi}(\mathbf{q}, t)$ is the momentum space mean-field. This is shown in figure 11(a), compared with measurements from [9] (red $\circ$) and corresponding simulations for our usual parameters. As we found earlier there is no big difference between mean-field and TWA results regarding the total number of fast atoms above the momentum cutoff, and both are in decent agreement with experiment up to a factor of two.

Additionally we show the total number of uncondensed atoms for the same scenarios in panel (b), sampled at the times indicated by markers. These all have higher momenta than q_{cut}. We thus see that a significant fraction of high-momentum atoms is uncondensed, while we also see that about half the atoms that exit the imaging region and thus contribute to the observation of loss have remained in the BEC.

5. Conclusions

We presented an extensive campaign of simulations of BEC dynamics in response to the excitation of multiple or single Rydberg atoms. We have described the quantum dynamics across all relevant length scales, ranging from microscopic scales within individual nanometer-sized radial wells of the Rydberg-BEC interaction potential, out to mesoscopic distances of twice the Rydberg orbital radius. We find that, while the dynamics within the Rydberg orbit is sensitive to the level of detail used to describe that interaction potential, density perturbations travelling outwards at later times are well reproduced also when using approximate interaction potentials, dramatically simplifying simulations.

We explored the shape and contrast of density perturbations as the number of Rydberg insertions is increased, and found that the typical response is the transient development of a density depression surrounding a density increase at the centre of the Rydberg excitation volume. The contrast of this feature

grows linearly with the number of Rydberg insertions. While signal in condensate density created by a single Rydberg atom remains very weak, it steadily increases if atoms are excited repeatedly. Importantly, we find that even after cessation of the excitation sequence, the signal increases further for a while as outgoing density waves combine. This suggests an additional unperturbed evolution interval as a helpful experimental tool to allow the Rydberg excitations to strongly affect the BEC.

Finally we went beyond mean-field theory, adding quantum fluctuations and the possibility of atoms being ejected from the condensate, using the TWA [47–53]. We find that a Rydberg impurity excited in the BEC causes additional uncondensed atoms, largely concentrated in the excitation region. The number of uncondensed atoms increases during a sequence of repeated excitations of a Rydberg impurity, but does not become large enough to invalidate the use of mean-field simulations and hence any of the conclusions listed above.

While we find that small scale details of the Rydberg-BEC potential, such as the p-wave shape resonance and radial oscillations, do not qualitatively affect the BEC response, larger features such as the anisotropy of p or d states [16], or transitions to molecules [22] represent a major change of the Rydberg-BEC potential and should leave a discernible signature after repeated excitations. Also different condensate atom species might give valuable information, such as *Sr* for which the shape resonance is absent, and *Cs*, the different mass of which will alter kinematics. All these should be subject of further investigations.

Two central conclusions are, that mean-field theory remains applicable to the Rydberg electron in a BEC, and that the detailed shape of the interaction potential at short distances, which is not too well known, is not crucial. Together, these findings provide a critical milestone that enables BEC as an instrument for *in situ* real time probing of dynamical processes in ultracold atomic physics and chemistry, ranging from polaron formation dynamics [3–5] over angular momentum changing collisions [15, 22], the dynamical formation of ultra-long range molecules [22, 24, 55], or localized states [56] and ionisation [57–60] to phonon mediated Yukawa interactions [61]. In all of these, the initially excited Rydberg atom can be in an s-state, on which we focus here, while cold scattering processes might then causes state changes or acceleration of this atom. These would likely leave an optically resolvable mark in the condensate response, since we show that already the s-state does. The highly excited atom in the BEC medium is somewhat analogous to exotic particles probed in bubble or fog chambers in the early days of particle physics [15, 20]. In that sense the present work provides the essential background simulations, by comparison with which all new discoveries arise, rendering much of the physics above *in situ* observable.

Acknowledgments

ST and SW thank the Max-Planck society for financial support through the MPG-IISER partner group program. FM acknowledges funding from Deutsche Forschungsgemeinschaft [Project No. PF 381/17-2, part of the SPP 1929 (GiRyd)], the Carl Zeiss Foundation via IQST, and is indebted to the Baden-Württemberg-Stiftung for the financial support by the Eliteprogramm for Postdocs. RS and MW acknowledge support by the Max Planck Society, the Deutsche Forschungsgemeinschaft (DFG, German Research Foundation) under Germany's Excellence Strategy EXC-2111-390814868 and within the priority programme 'Giant interactions in Rydberg systems', DFG SPP 1929 GiRyd, Grant No. 428462134.

Data availability statement

The data that support the findings of this study are available upon reasonable request from the authors.

Appendix A. Rydberg excitation locations

The location of a Rydberg excitation in a dense BEC can be controlled by a combination of a tightly focussed excitation beam and the Rydberg state energy dependence on background density [9]. To obtain an experimentally relevant spatial distribution of Rydberg excitations within a harmonically confined BEC, we model the excitation process taking these two features into account.

We start by generating clouds of point-like particles with a distribution function matching the Thomas–Fermi profile of the BEC density $\rho(\mathbf{R})$ in a cigar shaped harmonic trap, with long axis along y. In cylindrical coordinates

$$\rho(r,y,\phi) = \frac{1}{U_0}\left(\mu - \frac{m}{2}(\omega_r^2 r^2 + \omega_y^2 y^2)\right) \times \Theta\left(\mu - \frac{m}{2}(\omega_r^2 r^2 + \omega_y^2 y^2)\right), \tag{A.1}$$

where Θ is a Heaviside step function, $r = \sqrt{x^2 + z^2}$ (in this appendix only), μ the chemical potential and we assume trapping frequencies ω_r in the radial direction and ω_y along the long axis of the BEC. Note, that the Thomas Fermi profile is used in this appendix only, while the main article assumes a homogenous background BEC.

From the density distribution we can derive the corresponding cumulative distribution functions (CDFs) for each coordinate that allow us to randomly draw particle positions matching the probability to find atoms at a certain position inside the BEC. The extension of the BEC in the long direction is between $y_{\max} = -y_{\min} = \sqrt{2\mu/(m\omega_y^2)}$, and then for each y an upper bound for the radial coordinate is given by $r_{\max}(y) = 1/\omega_r \sqrt{2\mu/m - \omega_y^2 y^2}$. Consequently, the total particle number of the BEC is given by

$$N = \int_{y_{\min}}^{y_{\max}} \mathrm{d}y \underbrace{\int_0^{r_{\max}(y)} \mathrm{d}r \underbrace{\int_0^{2\pi} \mathrm{d}\phi\, r\, n(r,y,\phi)}_{=\bar{n}_\phi(r,y)}}_{=\bar{n}_{r,\phi}(y)}, \tag{A.2}$$

where $\bar{n}_{r,\phi}(y)\,\mathrm{d}y$ gives the weight of a disc with thickness $\mathrm{d}y$ (i.e. a cross-section of the BEC) and $\bar{n}_\phi(r,y)\,\mathrm{d}y\,\mathrm{d}r$ characterizes the weight of a infinitesimal cylinder of radius r for a given value of y. Based on the latter, the CDF of the y-coordinate is given by

$$\mathrm{CDF}_{n_{r,\phi}}(y) = \frac{1}{N} \int_{y_{\min}}^{y} \mathrm{d}y'\, \bar{n}_{r,\phi}(y'). \tag{A.3}$$

It maps the allowed range of y onto the interval $[0,1]$. Hence we can use the inverse CDF to draw random numbers $\xi_y^* \in [0,1]$ and assign them to y-coordinates y^*, which are then correctly distributed according to the Thomas–Fermi profile of the BEC. Analogously, we obtain the CDF of the radial coordinate

$$\mathrm{CDF}_{\bar{n}_\phi}(r,y)|_{y=y^*} = \frac{1}{N} \int_0^{r} \mathrm{d}r'\, \bar{n}_\phi(r',y)\,|_{y=y^*}. \tag{A.4}$$

The inverse of $\mathrm{CDF}_{\bar{n}_\phi}(r,y^*)$ assigns a random variable $\xi_r^* \in [0,1]$ to an r-coordinate r^* under the condition that the atom is found at the y-coordinate y^*, which has been obtained in the previous step. Finally the ϕ-coordinate is drawn uniformly from the interval $[0,2\pi)$, as the density profile (A.1) of the BEC is invariant under rotation around the y-axis. By successively drawing random coordinates as described above, we obtain 3D atom positions forming a cloud that matches the density distribution of a BEC confined in a harmonic trap. In the following we describe how to select atoms from this cloud to be excited into a Rydberg state by a Gaussian laser beam with a Gaussian profile and exploiting the density detuning of the energy of the Rydberg state.

The overall excitation probability is proportional to the intensity profile of the Gaussian beam which propagates anti-parallel to the x-axis of our coordinate system, see figure 1(a). To implement this, we evaluate the laser intensity profile

$$I(r_\perp, x) = I_0 \frac{\omega_0^2}{\omega(x)^2}\, \mathrm{e}^{-\frac{2r_\perp^2}{\omega(x)^2}} \tag{A.5}$$

at each atom within the cloud, where $r_\perp = \sqrt{y^2 + z^2}$, $\omega(x) = \omega_0 \sqrt{1 + x/x_R}$ and $x_R = \pi/\lambda\, \omega_0^2$ [62]. In accordance with a typical experimental setup, we choose $\omega_0 = 1.8\ \mu$m and $\lambda = 1.011\ \mu$m. We keep I_0 dimensionless and determine it such that the sum of the $I = (r_\perp, x)$ at all atom positions is normalized to one. Assuming the excitation of exactly one Rydberg atom, the function I can then directly be taken as the excitation probability of an atom at location $(r_\perp, x)$. This allows to select atoms to be excited into a Rydberg state according to the Gaussian intensity profile of the excitation laser.

In addition the dependence on light intensity, the excitation probability of an atom into a Rydberg state is density selective. This is because the spectral width of the laser only allows for excitations within a certain energy range ΔE, and interactions between the Rydberg atom and the BEC, as in section 2.1, cause an energy shift of the Rydberg state. We assume a Gaussian line shape of the excitation laser and hence a dependence of the excitation probability on energy shift E as

$$p(E) = \mathcal{N}\, \mathrm{e}^{-\frac{(E-\bar{E})^2}{\Delta E^2}}, \tag{A.6}$$

with $\Delta E = 1$ MHz centered around a detuning $\bar{E} = -55$ MHz. If the normalisation factor $\mathcal{N}$ is chosen such that $p(-55\ \mathrm{MHz}) = 1$, this assigns a probability to each excitation with energy detuning E. For each atom,

E is found by summing the potential energy shift due to the potential (2) for all other atoms in the cloud:

$$p(E) = \sum_k V_{\mathrm{ryd,S+P}}(\mathbf{R}_k). \tag{A.7}$$

Here $\mathbf{R}_k$ is the location of the kth cloud atom and we set $\eta(t) = 1$ and $\mathbf{x}_{n(t)}$ to the location of the atom for which we wish to evaluate the Rydberg excitation probability.

Finally the total Rydberg excitation probability for each atom in the cloud is given by $I(r_\perp, x) \times p(E)$. The histogram of excitation positions is well fitted by a three-dimensional Gaussian distribution, with the widths $\sigma_{x,y,z}$ given in the main text.

Appendix B. Rydberg molecular potentials

Since the interaction potential between the condensate and Rydberg impurity is solely governed by the electron–atom collision energy, a low energy Rydberg electron interacts with atoms through the Fermi pseudo potential [23, 24]:

$$W_{\mathrm{ryd,s},n}(\mathbf{R}, \mathbf{r}, t) = \eta(t) \left[V_0(\mathbf{R}) \delta^{(3)}(\mathbf{R} - \mathbf{x}_n(t) - \mathbf{r}) \right], \tag{B.1}$$

where $\mathbf{R}$ is the position of the ground state atom, $\mathbf{r}$ is the position of the Rydberg electron relative to the Rydberg core, and the latter is located at $\mathbf{x}_n(t)$. As the electron gets closer to the ionic core, it gains more kinetic energy from the Coulomb potential, that eventually matches with energy of a quasi-bound Rb^- state behind the p-wave centrifugal barrier [29]. This causes a shape resonance in the scattering cross-section between electrons and ^{87}Rb atoms in the $^3P^0$ scattering channel at 0.02 eV [29]. As a result, the Fermi pseudo-potential (B.1) needs to be extended to include p-wave scattering terms [30] as in

$$W_{\mathrm{ryd,s+p},n}(\mathbf{R}, \mathbf{r}, t) = \eta(t) \left[V_0(\mathbf{R}) \delta^{(3)}(\mathbf{R} - \mathbf{x}_n(t) - \mathbf{r}) \; + \frac{6\pi\hbar^2 a_{\mathrm{p}}[k(\mathbf{R})]}{m_{\mathrm{e}}} \delta^{(3)}(\mathbf{R} - \mathbf{x}_n(t) - \mathbf{r}) \overleftarrow{\nabla}_{\mathbf{r}} \cdot \overrightarrow{\nabla}_{\mathbf{r}} \right]. \tag{B.2}$$

Gradients act into the direct indicated by arrows. $\eta(t) = 1$ encapsulates the presence or absence of a Rydberg impurity in the BEC, and the first term in the square bracket is the usual s-wave pseudopotential (B.1), which upon taking the expectation value in the Rydberg state in the absence of the p-wave scattering term, results in the effective mean-pseudo-potential (1) defined in section 2.1. The last line of (B.2) is the p-wave scattering term, with p-wave scattering volume $a_{\mathrm{p}}[k(\mathbf{R})] = -\tan(\delta^{\mathrm{p}}[k(\mathbf{R})])/k(\mathbf{R})^3$, where $\delta^{\mathrm{p}}[k(\mathbf{R})]$ denotes the triplet p-wave scattering phase shift of e^-–$Rb^{87}(5S)$ [25]. In order to calculate the full Born–Oppenheimer potential energy surfaces of Rydberg electron–atom interaction from (B.2), we apply degenerate perturbation theory, diagonalising the Rydberg atom Hamiltonian as in (2) including the interaction (B.2) as a function of distance $r = |\mathbf{R}|$ between perturber atom and Rydberg ion. For each diagonalization, a total of six different ν manifolds and their respective angular momentum states have been taken into account, where one of them is above the target state and five are below. The angular momentum states for $l \leqslant 2$ are calculated using Numerov's algorithm to account for the quantum defect [27, 28], whereas hydrogenic basis states are utilized for higher angular momentum states. Finally we take an unusual choice of energy as a function of pertuber-ion distance following diagonalisation: since about $N_{\mathrm{orb}} = 8000$ perturbers already pre-fill the Rydberg electron orbit directly after excitation, the standard approach of adiabatically following the asymptotic s-state for all r is in-appropriate. Instead we heuristically follow it across the large energy drop induced by the p-wave coupling, to capture that acceleration, but at even closer distances return to the diabatic s-state. This is assuming that the high-dimensional Rydberg wavefunction as a function of the $3^{N_{\mathrm{orb}}}$-dimensional position of all perturbers is locally projected onto the largest s-state content through the excitation. We have verified that if the adiabatic potential is used for all radii up to $r = 0$ instead, our results e.g. in figures 3(c) and (d) are unchanged, due to the insensitivity to the details of the short range potential discussed in section 3.2.

The thus extracted potential energy for the surface asymptoting to $|\nu l\rangle = |133S\rangle$ is compared in figure 1(c) with the more basic s-wave scattering potential (1). A complete calculation of the $3^{N_{\mathrm{orb}}}$-dimensional surfaces for the $N_{\mathrm{orb}} = 8000$ perturbers in the orbit is not numerically feasible, and incompatible with mean-field theory. Since we expect a genuine many-body treatment to only differ sufficiently close to the p-wave resonance, and most of our results are not sensitive to even large potential variations in that range, the approach described should furnish a sufficient approximation.

As discussed in (3), for a simpler Rydberg-ground-state potential, we also make use of the classical electron probability distribution [32] given by

$$\rho^{\rm cl}(\mathbf{R}) = \frac{1}{8\pi^2 r}\frac{1}{\sqrt{\epsilon^2 b^2 - (r-b)^2}}, \tag{B.3}$$

where $r = |\mathbf{R}|$, $b = -k/2E$ is the semi-major axis for the elliptical electron orbit in a Coulomb field $U(\mathbf{R}) = -k/r$ with E the energy of the νth level and $\epsilon = \sqrt{1 + 2EL^2/m_e k^2}$ the eccentricity. Here L is the angular momentum of the Rydberg state and m_e is the mass of the electron.

Appendix C. Radial Gross–Pitaevskii equation in a homogeneous system

In section 3.1 we need to solve the radial GPE (5) to fully resolve the many small scale oscillations of the Rydberg-molecular potential. We wish to evaluate the derivatives in the GPE using the FFT algorithm, which implicitly enforces spatial periodicity. This is not straightforwardly possibly for a radial coordinate $r \in [0, R_{\rm max}]$ and a homogenous BEC background. A radial wavefunction $u(r)$ that vanishes at $R_{\rm max}$ can be propagated by anti-symmetrically extending it into $[-R_{\rm max}, 0]$. Since $u(r)$ does not vanish there for us, we work with a shifted radial wavefunction

$$\tilde{u}(r,t) = u(r,t) - r\sqrt{\rho}\,\mathrm{e}^{-\mathrm{i}\mu t/\hbar} \tag{C.1}$$

that is designed such that $\tilde{u}(r,t) = 0$ at large r, where the background is unperturbed. In the above, $\mu = U_0\rho_0$ is the chemical potential.

The new radial GPE for the variable $\tilde{u}(r,t)$ is then:

$$\begin{aligned}
\mathrm{i}\hbar\frac{\partial}{\partial t}\tilde{u}(r,t) = &-\frac{\hbar^2}{2m}\frac{\partial^2}{\partial r^2}\left(\tilde{u}(r,t)\right) \\
&+\left(\frac{U_0}{r^2}\left|\tilde{u}(r,t) + r\sqrt{\rho}\,\mathrm{e}^{-\mathrm{i}\mu t/\hbar}\right|^2 + V_{Ryd,S,n}(r)\right)\tilde{u}(r,t) \\
&+\left(\frac{U_0}{r^2}\left|\tilde{u}(r,t) + r\sqrt{\rho}\,\mathrm{e}^{-\mathrm{i}\mu t/\hbar}\right|^2\right. \\
&\left.+\,V_{\rm Ryd,S,}{}_n(r)\right) r\sqrt{\rho}\,\mathrm{e}^{-\mathrm{i}\mu t/\hbar} - r\mu\sqrt{\rho}\,\mathrm{e}^{-\mathrm{i}\mu t/\hbar},
\end{aligned} \tag{C.2}$$

where we have used that the actual 3D density is $\rho(r,t) = |\frac{u(r,t)}{r}|^2 = |\frac{\tilde{u}(r,t)+r\sqrt{\rho}\,\mathrm{e}^{-\mathrm{i}\mu t/\hbar}}{r}|^2$.

Working with an asymptotically vanishing $\tilde{u}(r,t)$ was required for the final step, which is to anti-symmetrically expand $\tilde{u}(r,t)$ to negative r, such that $\tilde{u}(-r) = -\tilde{u}(r)$. This enforces $\frac{\partial^2}{\partial r^2}|_{r=0} = 0$, thus preventing any cross-talk between the physical positive $r > 0$ and the unphysical negative range.

We verified the above transformations by a direct comparison of its results with complete 3D simulations for a Gaussian potential,

$$V(\mathbf{R}, \mathbf{x}_n, t) = V_0\,\mathrm{e}^{-\frac{|\mathbf{R}-\mathbf{x}_n(t)|^2}{2\tilde{\sigma}^2}}, \tag{C.3}$$

where V_0 and $\tilde{\sigma}$ are potential strength and width, finding good agreement as in figures C1(a) and (b). We then used these simulations to assess the impact of (unavoidable) undersampling of the Rydberg potential for 3D simulations in the main article in figures C1(c) and (d). While differences at early times $t_{\rm exc} + t_{\rm imp} = 4.0\ \mu$s in panel (c) can be significant, this is no longer the case for the net impact at large distances and late times $\tau + t_{\rm imag} = 231\ \mu$s, which is our main focus.

Appendix D. Truncated Wigner method

The truncated Wigner method allows to investigate the dynamics of quantum depletion or thermal fluctuation, as long as these are small corrections to a strong mean-field. After the method's introduction to BEC [47–49] the TWA in that context is described in many articles including the review [63]. The central ingredient of the method is adding random noise to the initial state of the GPE (4). We thus use the initial *stochastic field*

$$\alpha(\mathbf{R}, 0) = \phi_0 + \sum_k \left[\eta_k u_k(\mathbf{R}) - \eta_k^* v_k^*(\mathbf{R})\right]/\sqrt{2} \tag{D.1}$$

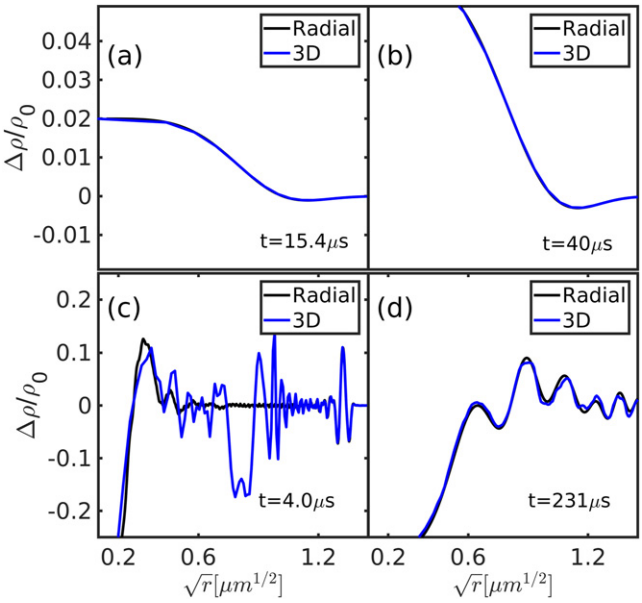

Figure C1. A direct comparison of solutions of the radial GPE (5) (blue lines) with the 3D GPE (4) (black lines). (a) and (b) Different time samples of the relative density of radial simulations and a 1D cut of the 3D simulation along the x-direction at $y = z = 0$, for the Gaussian potential in (C.3). (c) The relative density of the two simulations as in (a) and (b), with Rydberg s-wave potential (1) at $t_{\rm exc} + t_{\rm imp} + t_{\rm ion} = 4.0\ \mu$s. 60 000 grid points are used for the radial GPE simulation, whereas the 3D GPE simulation uses $512 \times 512 \times 512$ grid points along x, y, and z-directions, respectively. (d) Late time evolution of the relative density of the two simulations as in (c) at $\tau + t_{\rm imag} = 231\ \mu$s.

with random complex Gaussian noises η_k fulfilling $\overline{\eta_k \eta_l} = 0$ and $\overline{\eta_k \eta_l^*} = \delta_{nl}$, where $\overline{\cdots}$ is a stochastic average. $u_k(\mathbf{R})$ and $v_k(\mathbf{R})$ are the usual (3D) Bogoliubov modes in a homogeneous BEC with homogenous density $\rho = |\phi_0|^2$ [64].

A different symbol $\alpha(\mathbf{R})$ has been chosen for the stochastic field compared to the mean field $\phi(\mathbf{R})$, to emphasise the difference in physical interpretation due to the presence of noise: the stochastic field now allows the approximate extraction of quantum correlations using the prescription

$$\frac{1}{2}\left(\langle\hat{\Psi}^\dagger(\mathbf{R}')\hat{\Psi}(\mathbf{R})\rangle + \langle\hat{\Psi}(\mathbf{R})\hat{\Psi}^\dagger(\mathbf{R}')\rangle\right) \to \overline{\alpha^*(\mathbf{R}')\alpha(\mathbf{R})}, \tag{D.2}$$

in which spatial correlations of the stochastic fields provide information on *symmetrically ordered* quantum expectation values. In (D.2) $\hat{\Psi}(\mathbf{R})$ is the atomic field operator that destroys an atom at location $\mathbf{R}$ [64].

Using restricted basis commutators $\delta_{\rm c}$ [65, 66], we can then extract the total atom density

$$\rho_{\rm t}(\mathbf{R}) = \overline{|\alpha(\mathbf{R})|^2} - \frac{\delta_{\rm c}}{2}, \tag{D.3}$$

condensate density $\rho_{\rm c}(\mathbf{R}) = |\,\overline{\alpha(\mathbf{R})}\,|^2$ and from these both the uncondensed density $\rho_{\rm u}(\mathbf{R}) = \rho_{\rm t}(\mathbf{R}) - \rho_{\rm c}(\mathbf{R})$, see also [50–52]. Uncondensed atom numbers as a measure of non-equilibrium 'heating' referred to in the main article are finally $N_{\rm u} = \int {\rm d}^3\mathbf{R}\, \rho_{\rm u}(\mathbf{R})$.

ORCID iDs

S Tiwari https://orcid.org/0000-0002-6703-3945
M Wagner https://orcid.org/0000-0002-0428-7315
R Schmidt https://orcid.org/0000-0003-2776-269X
F Meinert https://orcid.org/0000-0002-9106-3001
S Wüster https://orcid.org/0000-0003-4382-5582

References

[1] Cyril Hewson A 1997 *The Kondo Problem to Heavy Fermions* (Cambridge: Cambridge University Press)
[2] Nakagawa M, Kawakami N and Ueda M 2018 Non-Hermitian Kondo effect in ultracold alkaline-earth atoms *Phys. Rev. Lett.* **121** 203001

[3] Grusdt F, Schmidt R, Shchadilova Y E and Demler E 2017 Strong-coupling Bose polarons in a Bose–Einstein condensate *Phys. Rev.* A **96** 013607
[4] Camargo F *et al* 2018 Creation of Rydberg polarons in a Bose gas *Phys. Rev. Lett.* **120** 083401
[5] Schmidt R *et al* 2018 Theory of excitation of Rydberg polarons in an atomic quantum gas *Phys. Rev.* A **97** 022707
[6] Bruderer M, Klein A, Clark S R and Jaksch D 2007 Polaron physics in optical lattices *Phys. Rev.* A **76** 011605
[7] Bruderer M, Klein A, Clark S R and Jaksch D 2008 Transport of strong-coupling polarons in optical lattices *New J. Phys.* **10** 033015
[8] Knap M, Shashi A, Nishida Y, Imambekov A, Abanin D A and Demler E 2012 Time-dependent impurity in ultracold fermions: orthogonality catastrophe and beyond *Phys. Rev.* X **2** 041020
[9] Balewski J B, Krupp A T, Gaj A, Peter D, Büchler H P, Löw R, Hofferberth S and Pfau T 2013 Coupling a single electron to a Bose–Einstein condensate *Nature* **502** 664
[10] Gaj A, Krupp A T, Balewski J B, Löw R, Hofferberth S and Pfau T 2014 From molecular spectra to a density shift in dense Rydberg gases *Nat. Commun.* **5** 4546
[11] Engel F, Dieterle T, Hummel F, Fey C, Schmelcher P, Löw R, Pfau T and Meinert F 2019 Precision spectroscopy of negative-ion resonances in ultralong-range Rydberg molecules *Phys. Rev. Lett.* **123** 073003
[12] Whalen J D, Camargo F, Ding R, Killian T C, Dunning F B, Pérez-Ríos J, Yoshida S and Burgdörfer J 2017 Lifetimes of ultralong-range strontium Rydberg molecules in a dense Bose–Einstein condensate *Phys. Rev.* A **96** 042702
[13] Schmidt R, Sadeghpour H R and Demler E 2016 Mesoscopic Rydberg impurity in an atomic quantum gas *Phys. Rev. Lett.* **116** 105302
[14] Mukherjee R, Ates C, Li W and Wüster S 2015 Phase-imprinting of Bose–Einstein condensates with Rydberg impurities *Phys. Rev. Lett.* **115** 040401
[15] Tiwari S and Wüster S 2019 Tracking Rydberg atoms with Bose–Einstein condensates *Phys. Rev.* A **99** 043616
[16] Karpiuk T *et al* 2015 Imaging single Rydberg electrons in a Bose–Einstein condensate *New J. Phys.* **17** 053046
[17] Rammohan S, Tiwari S, Mishra A, Chauhan A K, Nath R, Eisfeld A and Wüster S 2020 Imaging the interface of a q-bit and its quantum-many-body environment (arXiv:2011.11022)
[18] Rammohan S, Chauhan A K, Nath R, Eisfeld A and Wüster S 2021 Tailoring Bose–Einstein-condensate environments for a Rydberg impurity *Phys. Rev.* A **103** 063307
[19] Sous J, Sadeghpour H R, Killian T C, Demler E and Schmidt R 2020 Rydberg impurity in a Fermi gas: quantum statistics and rotational blockade *Phys. Rev. Res.* **2** 023021
[20] Glaser D A 1952 Some effects of ionizing radiation on the formation of bubbles in liquids *Phys. Rev.* **87** 665
[21] Ketterle W, Durfee D S and Stamper-Kurn D 1999 Making, probing and understanding Bose–Einstein condensates (arXiv:9904034 [cond-mat])
[22] Schlagmüller M *et al* 2016 Ultracold chemical reactions of a single Rydberg atom in a dense gas *Phys. Rev.* X **6** 031020
[23] Fermi E 1934 Sopra lo spostamento per pressione delle righe elevate delle serie spettrali *Nuovo Cimento* **11** 157
[24] Greene C H, Dickinson A S and Sadeghpour H R 2000 Creation of polar and nonpolar ultra-long-range Rydberg molecules *Phys. Rev. Lett.* **85** 2458
[25] Eiles M T 2018 Formation of long-range Rydberg molecules in two-component ultracold gases *Phys. Rev.* A **98** 042706
[26] Bahrim C, Thumm U and Fabrikant I I 2001 ^{3}Se and ^{1}Se scattering lengths for e^{-} + Rb, Cs and Fr collisions *J. Phys. B: At. Mol. Opt. Phys.* **34** L195
[27] Han J, Jamil Y, Norum D V L, Tanner P J and Gallagher T F 2006 Rb nf quantum defects from millimeter-wave spectroscopy of cold ^{85}Rb Rydberg atoms *Phys. Rev.* A **74** 054502
[28] Li W, Mourachko I, Noel M W and Gallagher T F 2003 Millimeter-wave spectroscopy of cold Rb Rydberg atoms in a magneto-optical trap: quantum defects of the ns, np, and nd series *Phys. Rev.* A **67** 052502
[29] Fabrikant I I 1986 Interaction of Rydberg atoms and thermal electrons with K, Rb and Cs atoms *J. Phys. B: At. Mol. Phys.* **19** 1527
[30] Omont A 1977 On the theory of collisions of atoms in Rydberg states with neutral particles *J. Phys. France* **38** 1343
[31] Kleinbach K S 2018 Ions and electrons interacting with ultracold atoms: novel approaches based on Rydberg excitations *PhD Thesis* University of Stuttgart http://dx.doi.org/10.18419/opus-10042
[32] Martín-Ruiz A, Bernal J, Frank A and Carbajal-Dominguez A 2013 The classical limit of the quantum Kepler problem *J. Mod. Phys.* **4** 818
[33] Middelkamp S, Lesanovsky I and Schmelcher P 2007 Spectral properties of a Rydberg atom immersed in a Bose–Einstein condensate *Phys. Rev.* A **76** 022507
[34] Shukla V, Pandit R and Brachet M 2018 Particles and fields in superfluids: insights from the two-dimensional Gross–Pitaevskii equation *Phys. Rev.* A **97** 013627
[35] Söding J, Guéry-Odelin D, Desbiolles P, Chevy F, Inamori H and Dalibard J 1999 Three-body decay of a rubidium Bose–Einstein condensate *Appl. Phys.* B **69** 257
[36] Schemmer M and Bouchoule I 2018 Cooling a Bose gas by three-body losses *Phys. Rev. Lett.* **121** 200401
[37] Wüster S, Hope J J and Savage C M 2005 Collapsing Bose–Einstein condensates beyond the Gross–Pitaevskii approximation *Phys. Rev.* A **71** 033604
[38] Savage C M, Robins N P and Hope J J 2003 Bose–Einstein condensate collapse: a comparison between theory and experiment *Phys. Rev.* A **67** 014304
[39] Dobrek Ł, Gajda M, Lewenstein M, Sengstock K, Birkl G and Ertmer W 1999 Optical generation of vortices in trapped Bose–Einstein condensates *Phys. Rev.* A **60** R3381
[40] Dennis G R, Hope J J and Johnsson M T 2012 http://xmds.org/
[41] Dennis G R, Hope J J and Johnsson M T 2013 XMDS2: fast, scalable simulation of coupled stochastic partial differential equations *Comput. Phys. Commun.* **184** 201
[42] Wilkie J and Çetinbaş M 2005 Variable-stepsize Runge–Kutta methods for stochastic Schrödinger equations *Phys. Lett.* A **337** 166
[43] Müller H, Chiow S-w and Chu S 2008 Atom-wave diffraction between the Raman–Nath and the Bragg regime: effective Rabi frequency, losses, and phase shifts *Phys. Rev.* A **77** 023609
[44] Wilson K E, Newman Z L, Lowney J D and Anderson B P 2015 *In situ* imaging of vortices in Bose–Einstein condensates *Phys. Rev.* A **91** 023621
[45] Vestergaard Hau L, Busch B D, Liu C, Dutton Z, Burns M M and Golovchenko J A 1998 Near-resonant spatial images of confined Bose–Einstein condensates in a 4-Dee magnetic bottle *Phys. Rev.* A **58** R54

[46] Gericke T, Würtz P, Reitz D, Langen T and Ott H 2008 High-resolution scanning electron microscopy of an ultracold quantum gas *Nat. Phys.* **4** 949
[47] Steel M J, Olsen M K, Plimak L I, Drummond P D, Tan S M, Collett M J, Walls D F and Graham R 1998 Dynamical quantum noise in trapped Bose–Einstein condensates *Phys. Rev.* A **58** 4824
[48] Sinatra A, Lobo C and Castin Y 2001 Classical-field method for time dependent Bose–Einstein condensed gases *Phys. Rev. Lett.* **87** 210404
[49] Sinatra A, Lobo C and Castin Y 2002 The truncated Wigner method for Bose-condensed gases: limits of validity and applications *J. Phys. B: At. Mol. Opt. Phys.* **35** 3599
[50] Wüster S, Daębrowska-Wüster B J, Bradley A S, Davis M J, Blakie P B, Hope J J and Savage C M 2007 Quantum depletion of collapsing Bose–Einstein condensates *Phys. Rev.* A **75** 043611
[51] Wüster S, Daębrowska-Wüster B J, Scott S M, Close J D and Savage C M 2008 Quantum-field dynamics of expanding and contracting Bose–Einstein condensates *Phys. Rev.* A **77** 023619
[52] Daębrowska-Wüster B J, Wüster S and Davis M J 2009 Dynamical formation and interaction of bright solitary waves and solitons in the collapse of Bose–Einstein condensates with attractive interactions *New J. Phys.* **11** 053017
[53] Norrie A A, Ballagh R J, Gardiner C W and Bradley A S 2006 Three-body recombination of ultracold Bose gases using the truncated Wigner method *Phys. Rev.* A **73** 043618
[54] Balewski J B 2014 A single electron in a Bose–Einstein condensate *PhD Thesis* University of Stuttgart
[55] Luukko P J J and Rost J-M 2017 Polyatomic trilobite Rydberg molecules in a dense Random gas *Phys. Rev. Lett.* **119** 203001
[56] Eiles M T, Eisfeld A and Rost J M 2021 Anderson localization of a Rydberg electron (arXiv:2111.10345 [cond-mat])
[57] Li W, Tanner P J and Gallagher T F 2005 Dipole–dipole excitation and ionization in an ultracold gas of Rydberg atoms *Phys. Rev. Lett.* **94** 173001
[58] Amthor T, Reetz-Lamour M, Westermann S, Denskat J and Weidemüller M 2007 Mechanical effect of van der Waals interactions observed in real time in an ultracold Rydberg gas *Phys. Rev. Lett.* **98** 023004
[59] Viteau M, Chotia A, Comparat D, Tate D A, Gallagher T F and Pillet P 2008 Melting a frozen Rydberg gas with an attractive potential *Phys. Rev.* A **78** 040704
[60] Park H, Shuman E S and Gallagher T F 2011 Ionization of Rb Rydberg atoms in the attractive nsnp dipole–dipole potential *Phys. Rev.* A **84** 052708
[61] Wang J, Gacesa M and Côté R 2015 Rydberg electrons in a Bose–Einstein condensate *Phys. Rev. Lett.* **114** 243003
[62] Siegman A E 1986 *Lasers* (Mill Valley, CA: University Science Books)
[63] Bradley P B, Bradley A S, Bradley M J, Davis R J, Ballagh C W and Gardiner C 2008 Dynamics and statistical mechanics of ultra-cold Bose gases using c-field techniques *Adv. Phys.* **57** 363
[64] Pethik C J and Smith H 2002 *Bose–Einstein Condensation in Dilute Gases* (Cambridge: Cambridge University Press)
[65] Norrie A A, Ballagh R J and Gardiner C W 2006 Quantum turbulence and correlations in Bose–Einstein condensate collisions *Phys. Rev.* A **73** 043617
[66] Norrie A A 2005 A classical field treatment of colliding Bose–Einstein condensates *PhD Thesis* University of Otago http://physics.otago.ac.nz/nx/jdc/jdc-thesis-page.html